Computers & Geosciences 182 (2024) 105463

Contents lists available at ScienceDirect

Computers and Geosciences

journal homepage: www.elsevier.com/locate/cageo

Automated mapping of bedrock-fracture traces from UAV-acquired images using U-Net convolutional neural networks

Bijal Chudasama [a,*], Nikolas Ovaskainen [a,b], Jonne Tamminen [c], Nicklas Nordbäck [a,b], Jon Engström [a], Ismo Aaltonen [a]

[a] Geological Survey of Finland, Vuorimiehentie 5, FI-02151, Finland
[b] Department of Geography and Geology, University of Turku, FI-20014, Finland
[c] Department of Mathematics and Statistics, University of Turku, FI-20014, Finland

ARTICLE INFO

Keywords:
Deep learning
Convolutional neural networks
U-Net
Semantic segmentation
Bedrock fractures
Automated fracture-trace mapping
UAV-Images
Loviisa islands
Finland

ABSTRACT

This contribution presents a novel U-Net convolutional neural network (CNN)-based workflow for automated mapping of bedrock fracture traces from 0.55 cm spatial resolution aerial photographs, acquired by unmanned aerial vehicles (UAV), over the Wiborg Rapakivi granite outcrops in the islands off the coast of the Loviisa Region in Southern Finland. The workflow comprised training a U-Net CNN using a small subset of photographs with manually traced fractures for optimizing the network parameters using the root mean squared propagation optimizer and sigmoidal focal loss function for semantic segmentation of input images and pixel-wise identification of fracture traces. The ridge detection algorithm was then applied to the U-Net prediction results, followed by vectorization of the fracture-traces pixels as vector polylines representing the traces of fractures. Both intensity values of the pixels and topological connectivity were used in the process of vectorization. Quantitatively the results were assessed using various accuracy assessment metrics. Qualitative evaluations of the results were implemented by comparisons of orientations and length-frequency distributions of automatically- and manually-mapped traces.

The results show that the model has the class-balanced accuracy score 0.945, predicting 88.79% of the fracture-trace pixels. Bedrock outcrops with well-exposed surfaces present high true positive rates (>99%). The demonstration (test) site has the class-balanced accuracy score of 0.873 and 75% true positive rate. Additionally, the fracture trace networks replicate the orientation distributions of the manually digitized traces. The length distributions of automatic traces, however, differ with varying intensity from the manual trace length distributions. However, this study demonstrates that the workflow can be successfully applied to UAV-acquired images for fast and efficient automated mapping of bedrock-fracture traces during the initial phases of structural characterization of a region.

1. Introduction

Granitic bedrock exposed in the Finnish archipelago, off the coast of the Loviisa region in southwestern Finland is part of the Wiborg Rapakivi Batholith (Vaasjoki et al., 1991; Rämö and Haapala, 2005). There are numerous islands with rapakivi outcrops in this region and identification of fracture patterns from the bedrock outcrops is an important pre-requisite for subsequent detailed fracture mapping. For instance, mapping of geological structures, topological network analysis and subsurface fracture modelling is crucial in applied fields of geoscientific research such as mineral exploration, groundwater flow modelling, mapping sites for CO_2 sequestration or nuclear waste disposal, bedrock stability analysis, hydrocarbon resources exploration, reservoir analysis and predictions of natural disasters such as landslides and earthquakes and associated mitigation planning.

Advances in the imaging of bedrock exposures using Unmanned Aerial Vehicles (UAVs) has facilitated rapid acquisition of large volumes of aerial photographs with high-spatial resolutions, (e.g.: Bemis et al., 2014; Dering et al., 2019; Honarmand and Shahriari, 2021; Nex et al., 2022; Samsu et al., 2020; Thiele et al., 2017, 2019; Turner et al., 2012). This enables digital mapping and evaluation of structural features in both 2D and 3D over large areas with up to centimeter-to-millimeter

* Corresponding author.
E-mail address: bijal.chudasama@gtk.fi (B. Chudasama).

https://doi.org/10.1016/j.cageo.2023.105463
Received 8 October 2022; Received in revised form 12 June 2023; Accepted 21 September 2023
Available online 1 October 2023

scale of spatial resolutions (e.g.: Ovaskainen et al., 2022; Samsu et al., 2020; Thiele et al., 2017, 2019). However, the UAV-based image acquisition process is an order of magnitude quicker in comparison to the subsequent image analysis for digitization and mapping of fracture traces which is furthermore subject to interpreter bias unique to the digitizer (Bond et al., 2007; Scheiber et al., 2015). Hence, obtaining an automated solution for mapping fracture traces from orthophotographs has gradually gained importance with the advancements in UAV-based image acquisition technology and processing workflows (Prabhakaran et al., 2019).

Over the years several studies have implemented semi-automated image-processing based methods to machine-learning-based automated mapping of structural features from seismic data (e.g.: Araya-Polo et al., 2017; Chopra et al., 2014; Guitton, 2018; Li et al., 2020; Lin et al., 2022; Tingdahl and De Rooij, 2005; Wu and Fomel, 2018; Wu et al., 2022; Zhang et al., 2019), aerial and ground geophysical measurement grids (e.g.: Thiele et al., 2017; Vasuki et al., 2014), satellite-based earth observation datasets (Aghaee et al., 2021; Lepage et al., 2000), digital elevation models (e.g.: Abdullah et al., 2010; Bonetto et al., 2017) and UAV-acquired or field-based outcrop images (e.g.: Prabhakaran et al., 2019; Vasuki et al., 2014). The conventional approaches involve image processing-based edge-detection filters and transformations such as Canny (1986), Sobel (Sobel, 1970; Sobel and Feldman, 2015; Vincent and Folorunso, 2009), Prewitt (1970), Robert (Roberts, 1965), Gabor filter (Weldon et al., 1996), Laplacian of Gaussian (Marr and Hildreth, 1980), Hough transform (Hough, 1962; Duda and Hart, 1972) and such others. Initially designed for single band grey scale images, these filters detect edges from the first- (e.g., gradient operators) and second-order (e.g., Laplacian operators) derivatives of the image intensity values. Hence, these methods have limitations because of variations in image brightness, magnification, and resolution. The threshold for the gradient values relating to edges is determined empirically or subjectively. Therefore Kovesi (1997 and 1999) proposed frequency-based Fourier transformation methods evaluating the phase symmetry and phase congruency of signal for detection of lines and edges in the images. For example, Vasuki et al. (2014) demonstrated the application of phase-symmetry (Kovesi, 1997) and phase-congruency analysis (Kovesi, 1999) methods for mapping of lineaments from geophysical datasets. However, the conventional methods are sensitive to noise, often leading to false edge detections. Machine learning-based methods can benefit from the derivative-based edges to learn the characteristics of the edge pixels (e.g.: Dollár and Zitnick, 2015; Hallman and Fowlkes, 2015; Wang et al., 2007). Another approach demonstrated by Prabhakaran et al. (2019) involves implementation of complex shearlet transform for automatic extraction of fracture traces. However, both machine learning-based methods and standard edge detection methods utilize linearity and gradient for tracing edges and boundaries. Hence, when applied to mapping faults- and fracture-traces, commonly interfering objects and patterns in the images lead to a high percentage of misclassifications. Therefore, current research in this field has immense potential to be leveraged by deep learning-based methods for mapping of fracture traces from different types of images.

Deep neural networks have been widely applied to different computer vision and pattern recognition applications such as biomedical image segmentation (e.g.: Havaei et al., 2017; D. Li et al., 2019; Milletari et al., 2017; Moeskops et al., 2016; Ronneberger et al., 2015; Roth et al., 2018), object detection and object segmentation (Badrinarayanan et al., 2017; Hariharan et al., 2014; 2016; He et al., 2017, 2022; Redmon et al., 2016; Ren et al., 2017; Sermanet et al., 2014; Shelhamer et al., 2017), change detection (e.g.: Gong et al., 2017; Sefrin et al., 2021; Varghese et al., 2019), image colorization and reconstructions (Cheng et al., 2015; Cheng et al., 2018; Iizuka et al., 2016; Van Oord et al., 2016; Zhang et al., 2016), image super-resolution (e.g.: Arun et al., 2019, 2020; Arun and Buddhiraju, 2016; Lai et al., 2017; Ledig et al., 2017) and other forms of image synthesis (e.g.: Gautam et al., 2022; Liu et al., 2022; Wang et al., 2019; Zhang et al., 2018). In the field of geosciences, a few studies have demonstrated the effectiveness of using different deep learning-based Convolutional Neural Networks (CNNs) for semantic segmentation and detection of fractures from 2D images. For instance, Chen et al. (2021) used a FraSegNet CNN for automated rock fracture segmentation and fracture trace quantification. Junior et al. (2021) implemented a comparative study of U-Net and Segnet CNNs for pixel-wise segmentation of fractures in UAV-images. Jafrasteh et al. (2020) and Manighetti et al. (2020) employed U-Net and Generative Adversarial Network (GAN) CNNs for automated tectonic fault mapping from optical images. Mattéo et al. (2021) and Kanoun et al. (2022) also implemented a U-Net CNN for automatic fault mapping from optical images and topographic data. Byun et al. (2021) used U-Net CNN for rock fracture image segmentation from ground-based field photographs. These studies demonstrate that deep learning-based methods are fast and effective for automated-mapping of fracture traces from different types of bedrock photographs. The main advantage of CNNs over conventional methods is that being guided by multi-level hierarchical feature detections, these networks can account for the multi-scale nature of edges, particularly faults and fracture traces. Edge-detection filters have discrete user-defined values in the kernels, but in deep CNNs, the network learns the appropriate filters and the kernel values at multiple scales based on topological relations and complex spatial dependencies of pixels in an image. Hence, in this study we use a deep learning-based approach for automated mapping of fracture traces from 2D orthomosaics derived from the UAV-acquired aerial photographs for real-world application.

Since the bedrock within the Finnish archipelago is well exposed, it offers ideal targets to acquire UAV-based imagery with high spatial resolution. Consequently, the Geological Survey of Finland has focused such surveys for 2D fault and fracture mapping in crystalline bedrock to the areas of the archipelago. Specifically, such imagery has been acquired from the outcrops of Loviisa (Ovaskainen, 2020; Skyttä et al., 2021), Åland Islands (Ovaskainen et al., 2022) and the Inkoo region (Nordbäck et al., 2023). Subsequent, detailed multi-scale fracture trace mapping and fracture network analysis for these outcrops has been conducted for identification and characterization of fracture patterns (e.g.: Ovaskainen, 2020; Ovaskainen et al., 2022) and for later use in e.g., paleostress interpretation. Studies have been targeted to rapakivi granitic rock, due the lithologically homogenous and structurally isotropic nature of this rock type. The study area has sufficient datasets for testing the capabilities of deep learning-based U-Net CNN for automated mapping of fracture traces from UAV-acquired images of bedrock outcrops. Furthermore, beyond just testing, the produced model can be applied to other rapakivi granitic outcrops in the Finnish archipelago (with similar weathering and visibility conditions) for automated, effective and rapid mapping of fracture traces from UAV-acquired images. Potentially, the same model can be applied to non-horizontal surfaces such as tunnel walls during bedrock construction.

To estimate the applicability of the automatically generated fracture traces in fracture network characterization, their intensity, lengths and orientations are compared to traces that are manually digitized from the same target areas. All three of these geometric properties of the fracture traces are important characteristics when considering the stability of the rock mass (Liu and Chen, 2007), preferred orientations and intensities of possible fluid flow (Neuman, 2005) and earthquake hazard estimation (Eliason, 1992). Quick and accurate automatic determination of these characteristics is valuable to e.g., bedrock construction and site assessment projects.

This study hence demonstrates a real-world application of CNNs and probes into the possible limitations and advantages for further development of this approach that can facilitate end-to-end automated mapping of bedrock-fracture traces from aerial imagery with consistent spatial resolution.

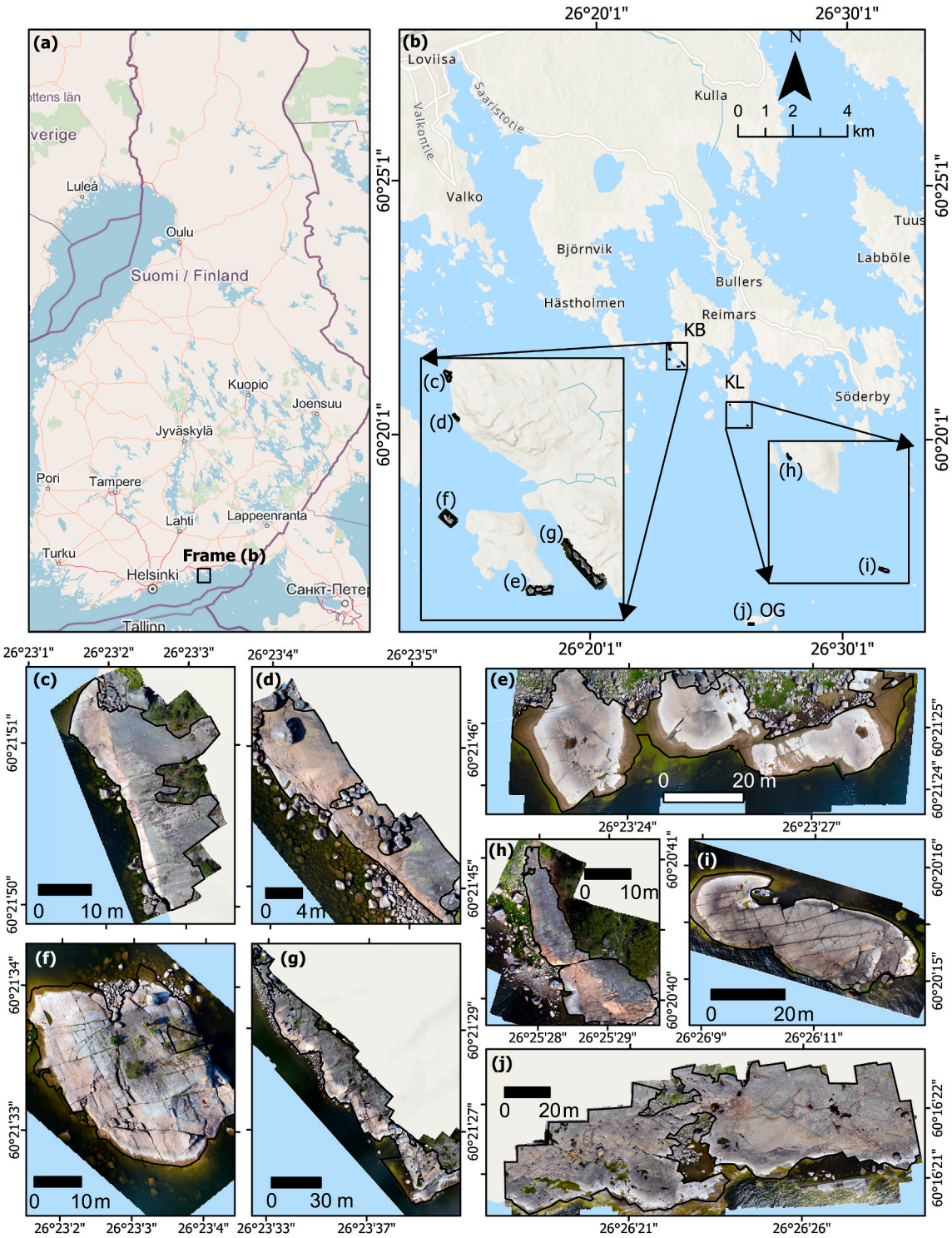

Fig. 1. (a) Geopolitical location of the study area in southwest Finland, (b) Detailed study area islands: Kasaberget (KB), Kampuslandet (KL) and Orrengrund (OG) islands off the coast of the Loviisa region, (c) Orthomosaic of outcrop KB7, (d) Orthomosaic of outcrop KB9, (e) Orthomosaic of outcrop KB2, (f) Orthomosaic of outcrop KB11, (g) Orthomosaic of outcrop KB3, (h) Orthomosaic of outcrop KL2_1, (i) Orthomosaic of outcrop KL5 and (j) Orthomosaic of outcrop OG1 on the Orrengrund island.

2. Study area

The study area comprises of islands along the coast of the Loviisa region in southeastern Finland which are located within the Wiborg Rapakivi Batholith. The batholith was emplaced in a N–S extensional regime between 1.65 and 1.62 Ga during which it intruded the older Precambrian basement (Vaasjoki et al., 1991; Rämö and Haapala, 2005; Haapala et al., 2005). As it post-dates the major tectonic deformation phase of the Svecofennian orogeny (Nironen, 1997) it lacks the pervasive ductile deformation which is common elsewhere in Finland and is therefore largely structurally isotropic without precursor fabrics. The batholith is furthermore lithologically homogeneous, macroscopically, without distinct contacts between rapakivi granite types. In the absence of precursor fabrics or ductile structures to control the brittle

Table 1
Training, validation and testing site (orthomosaics) details.

	Name	Area (m^2)	Number of fracture traces	Dominant Orientations (at drone/outcrop scale from 20 m flight altitude-based drone traces) (Ovaskainen, 2020; Skyttä et al., 2021)
Base Ref.	KL5	1237.9	919	ENE-WSW
Training Sites	KB2	1671.06	520	ENE-WSW, NNW-SSE
	KB3	3651.41	1219	ENE-WSW, NNW-SSE
	KB7	534.68	240	ENE-WSW
	KL2_1	418.55	730	N–S, ENE-WSW
	Total	6275.7	2709	
Validation Sites	KB9	163.77	234	ENE-WSW, NNW-SSE
	KB11	1237.9	708	ENE-WSW, NNW-SSE
	Total	1401.67	942	
Application Site	OG1	7001.56	2244	ENE-WSW, NW-SE

deformation, the fracture growth within the batholith can hence be assumed to be controlled by the regional stress field, making it ideal for studying fracture genesis. Furthermore, the overall homogeneity decreases the amount of patterns that could interfere with trace detection on the bedrock surface such as those caused by foliation or discrete layering, making the area suitable for testing purposes.

The sites in the Loviisa region that were selected for this study are the outcrops along the shore of the (i) Kasaberget (KB), (ii) Kampuslandet (KL) and (iii) Orrengrund islands (Fig. 1). Regional-scale lineament (lineament lengths approximately from 100 m to 200 000 m) and fracture (lengths approximately from 0.01 m to 100 m) analysis indicates the presence of three sets of structural trends in this region. These are NE-to-E-oriented Set 1 structures (with azimuth ranging from 45° – 90°), SE-to-S-oriented Set 2 structures (with azimuth ranging from 125° – 170°) and the nearly N–S oriented Set 3 structures (with azimuth ranging from 171° – 15°) (Ovaskainen, 2020). However, local variations in orientations occur at each site. For instance, set 3 is dominant in the Kampuslandet (KL) island sites. Table 1 summarizes the study area sites, the spatial extent, number of fracture traces and the orientation of the traces.

3. Data and methods

3.1. Data

This study uses the following two datasets: (i) orthomosaics of the aerial photographs acquired by a UAV in the visible region (0.4–0.7 μm) of the electromagnetic spectrum (Nordbäck and Ovaskainen, 2022), and (ii) fracture traces visually interpreted and manually digitized as polylines from the corresponding orthophotographs (Ovaskainen and Nordbäck, 2022).

The Loviisa region was photographed aerially by the Geological Survey of Finland using a DJI Phantom 4 Pro UAV at a flight altitude of 20 m and with a resulting ground spatial resolution of 0.55 cm per pixel. The image acquisition paths were designed to ensure 60–70% overlap between adjacent images. Ovaskainen (2020) and James (2017) describe the procedures used for relevant photogrammetric corrections of the aerial photographs to create the orthomosaics. Consequently, orthomosaics of eight outcrops from three sites (Table 1) and the corresponding fracture traces were used in this study. The fracture traces were initially digitized for a study on scalability of fracture traces in the Loviisa region by Ovaskainen (2020) and detailed procedures of mapped traces are described therein.

The data of fracture traces (Ovaskainen and Nordbäck, 2022) were used as training data for optimizing the U-Net CNN for classifying the image into the fracture-traces class and the background non-trace class. For the purpose of training, individual outcrop sites were divided into training sites (KL5, KB2, KB3, KB7, KL2_1), validation sites (KB9, KB11) and testing site (OG1) (Fig. 1). The orthomosaic of outcrop KL5 was first used to train a base reference model. This area was selected because of the well-exposed fracture traces and less surface cover (Fig. 1i). Following the training of the initial reference model, the orthomosaics of outcrops – KB2, KB3, KB7, and KL2_1, were used for further training and optimization of the network. Orthomosaics of outcrops KB9 and KB11 were used as validation sites. Finally, the outcrop, OG1 (Fig. 1j), from the Orrengrund island ~8 km south of the Kampuslandet island, was used for an independent prediction using the trained network. This tested the prediction capabilities and real-world testing of the method for automated mapping of fracture traces from UAV-acquired images.

The base-reference model for KL5 was trained using 1110 image tiles extracted from its orthomosaic. The training dataset contained 2148

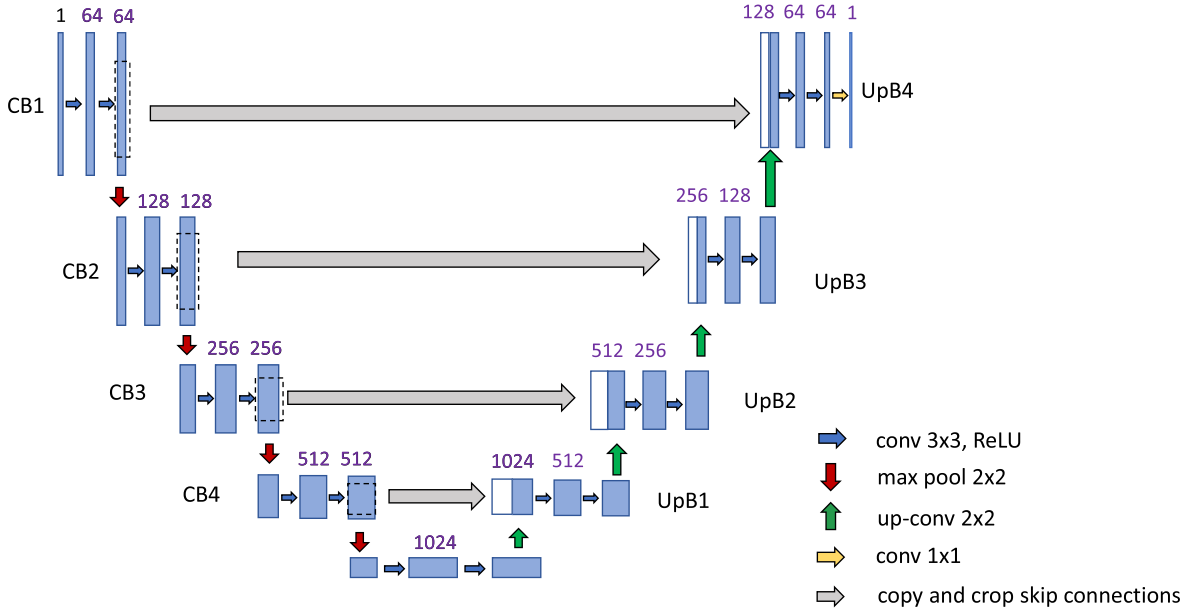

Fig. 2. Architecture of the U-Net CNN implemented in this study (modified after Ronneberger et al., 2015). Abbreviations: CB: Convolution Block; UpB: Upsampling Block.

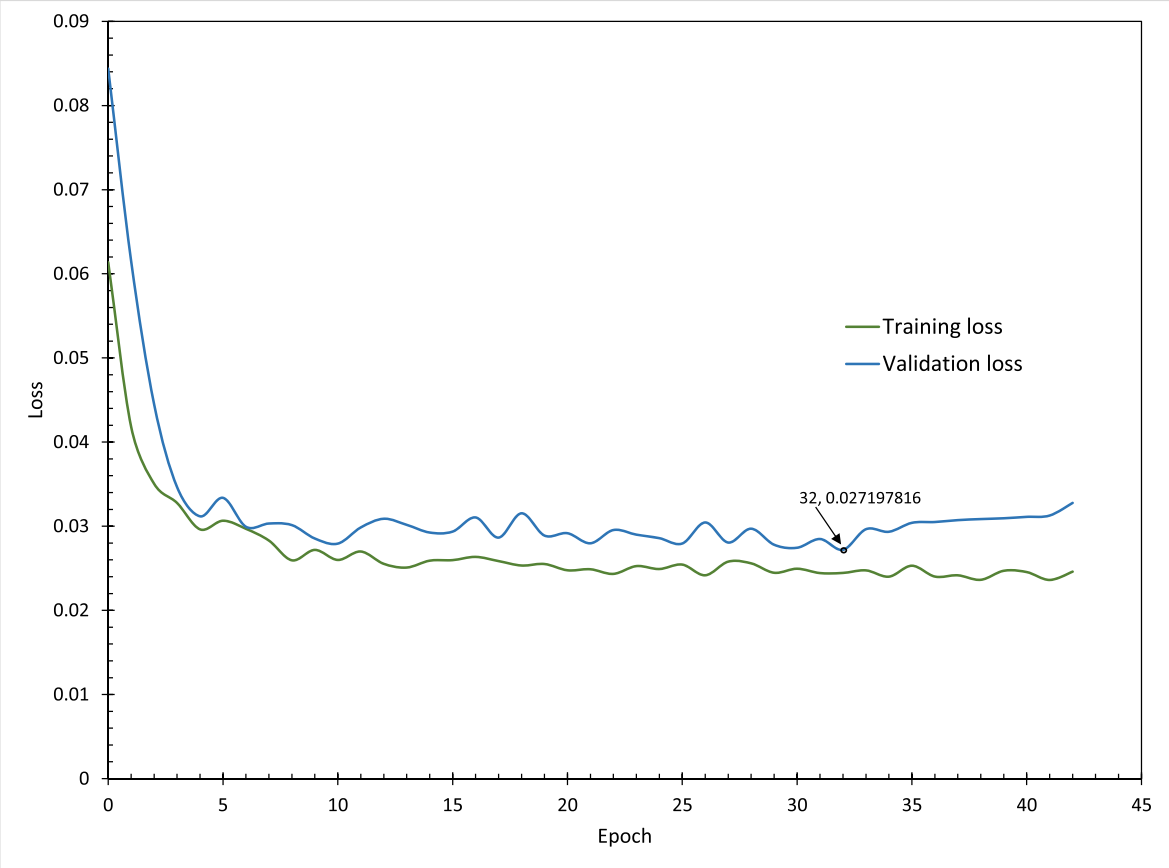

Fig. 3. Monitoring the optimization of the network during the training and validation steps per epoch.

image tiles, the validation dataset contained 1324 image tiles and the demonstration dataset had 842 images tiles; each tile sized as 256 × 256 pixels. Corresponding training-trace data was created from the digitized fracture traces. There were 919 traces for training the base-reference model, 2709 traces in the training set and 942 traces in the validation set (Table 1). A total of c. 1.3 M (1.5%) pixels coinciding with the manually digitized fracture traces were used as training samples for the traces class 1, and a total of c. 84 M (98.5%) pixels coinciding with the background outcrop area were used as training for the background 'non-trace' class 0.

3.2. Methods

This study uses a U-Net-architecture-based CNN for automated mapping of fracture traces from UAV-acquired aerial photographs. The method is adapted from Ronneberger et al. (2015) that introduced U-Net CNN for biomedical image segmentation. Application of U-Net CNNs for mapping of fracture traces from remotely acquired optical images is presented in a few studies (Tamminen, 2020; Mattéo et al., 2021; Jafrasteh et al., 2020; Manighetti et al., 2020; Junior et al., 2021). The method has also found application in fault-trace mapping from seismic data (e.g.: Lin et al., 2022; Wu et al., 2022; G. Li et al., 2020). Tamminen (2020) optimizes the U-Net model presented by Ronneberger et al. (2015) to mapping fracture traces from aerial images. The same methodology was used in this study.

The workflow involved the following steps:

(i) Data pre-processing
(ii) Training-validation and optimization of the U-Net CNN
(iii) Predictions on all orthomosaic images
  a. Processing of the images using the trained U-Net and obtaining probabilistic output for each pixel.
  b. Extraction of fracture traces from the pixels using the ridge detection algorithm
  c. Segmentation of the images into fracture-traces and background non-fracture trace pixels
  d. Vectorization of the fracture traces pixels as polylines representing the traces of fractures
  e. Post-processing of the vectorized fracture traces polylines
(iv) Results evaluation
  a. Quantitative accuracy assessments
  b. Network analysis and comparisons of orientations and length-frequency distributions

3.2.1. Experimental setup

Step (i) of data pre-processing and preparation was implemented in QGIS, it involved pre-processing steps including defining the study area boundary, clipping of the orthomosaics within the boundary ensuring that the 'no data' pixels are masked and exporting the clipped images as georeferenced Portable Network Graphics (PNG) image files. Steps (ii-iii) were implemented in the python environment using the codes published by Tamminen and Ovaskainen (2022). After the extraction and vectorization of the fracture traces (steps iii b-e), accuracy assessments metrics for individual sites were calculated in step (iv a) in GIS and python environments. Topological analysis and comparisons in step (iv b), were implemented according to the procedures described by Ovaskainen (2023, 2022) and Ovaskainen et al. (2022) using the corresponding python package.

The computations were performed on Microsoft Azure's cloud based D2-V4 series virtual machines (Microsoft, 2022) with a 64-bit Windows

Table 2
Individual area-wise accuracy assessment metrics for the results.

Area	TPR (Recall)[(i)]	Precision[(ii)]	Error of Commission for traces (%) [(iii)]	Error of Omission for traces (%) [(iv)]	Overall Accuracy (%) [(v)]	Balanced Accuracy [(vi)]	Kappa co-efficient [(vii)]	F1 score [(viii)]	MIoU[(ix)]
Training									
KB2	0.946	0.772	22.77	5.45	99.15	0.969	0.846	0.850	0.865
KB3	0.903	0.858	14.22	9.73	99.00	0.951	0.880	0.880	0.892
KB7	0.898	0.621	37.87	10.23	98.29	0.941	0.726	0.734	0.781
KL2_1	0.964	0.890	10.99	3.56	99.27	0.980	0.922	0.926	0.927
Total	0.920	0.810	18.85	7.65	99.41	0.961	0.860	0.810	0.879
Validation									
KB9	0.992	0.651	34.88	0.78	98.13	0.987	0.777	0.786	0.814
KB11	0.771	0.918	8.22	22.89	98.46	0.884	0.830	0.838	0.853
Total	0.802	0.858	14.22	19.84	98.40	0.897	0.820	0.829	0.845
Training + Validation	0.890	0.820	17.68	11.21	99.00	0.945	0.852	0.854	0.871
Testing									
OG1	0.752	0.811	18.90	24.84	98.70	0.873	0.774	0.780	0.813

Abbreviations: TPR = True Positive Rate, TP = True Positives, TN = True Negatives, FP = False Positives, FN = False Negatives, MIoU = Mean of Intersection of Unioin Accuracy Evaluation Metrics.

[(i)] TPR (Recall) $= \frac{TP}{TP + FN}$.

[(ii)] Precision $= \frac{TP}{TP + FP}$.

[(iii)] Error of commission for traces pixels (%) $= \frac{FP}{FP + TP} \times 100$.

[(iv)] Error of omission for traces pixels (%) $= \frac{FN}{FN + TP} \times 100$.

[(v)] Overall Accuracy (%) $= \frac{TP + TN}{Total\ numbaer\ of\ pixels}$.

[(vi)] Balanced Accuracy $= \frac{1}{2}\left(\frac{TP}{TP + FN} + \frac{TN}{TN + FP}\right)$.

[(vii)] Kappa co-efficient $= k = \frac{p_o - p_e}{1 - p_e}$, where p_o is the relative observed agreement and p_e is the hypothetical probability of chance agreement.

[(viii)] F1 score $= \frac{2 \times Precision \times Recall}{Precision + Recall}$.

[(ix)] MIoU $= \frac{1}{2}\left[\left(\frac{TP}{TP + FP + FN}\right) + \left(\frac{TN}{TN + FP + FN}\right)\right]$.

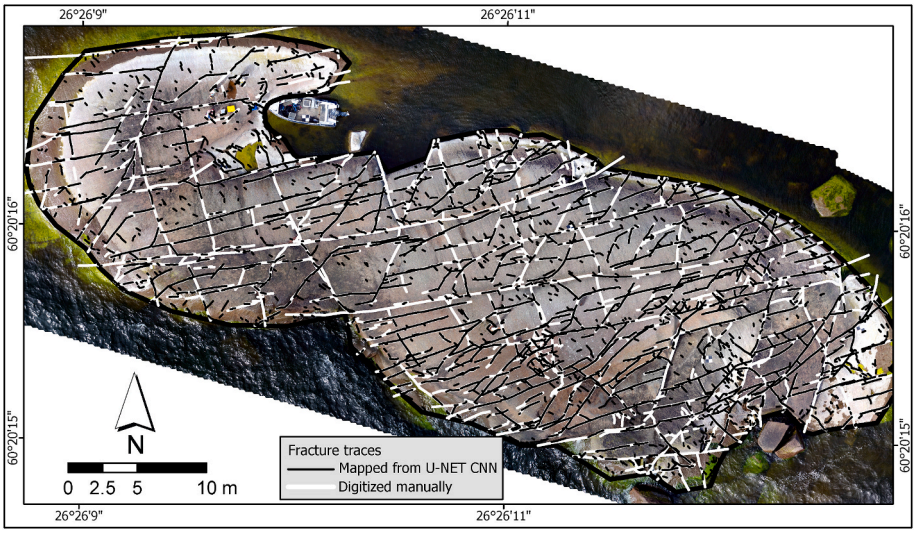

Fig. 4. Bedrock-fracture traces for the KL5 outcrop.

10 operating system, 8 GB installed RAM and 80 GB virtual memory, 2vcpus, 20 virtual processors. The system contained Intel® Xeon® Platinum 8272CL (Cascade Lake) @2.60 GHz processor in a hyper-threaded configuration (Intel® Hyper-Threading Technology, n. d.). With the above configuration the training operation took 5 s per step per epoch. For the current experiment the training configuration comprised of 300 training steps and 100 validation steps for each epoch. The maximum number of epochs was limited to 50. The predictions of

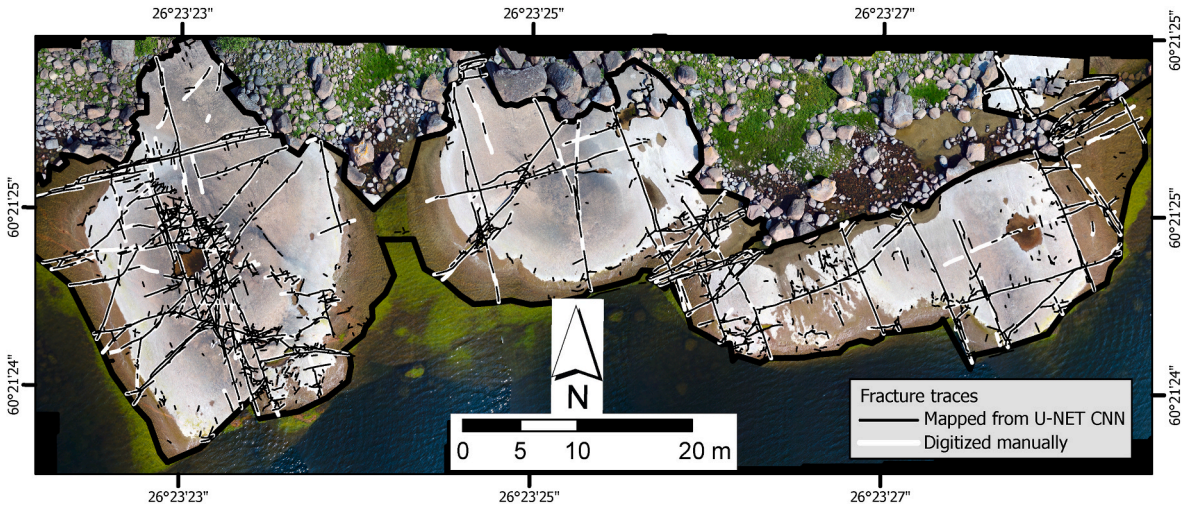

Fig. 5. Bedrock-fracture traces for the KB2 outcrop.

traces and subsequent vectorization for the prediction test site OG1 was computed in 18 mins.

3.2.2. Background to the U-net CNN

A U-Net CNN comprises two sub-networks, an encoder and a decoder, with skip connections between these units (Ronneberger et al., 2015). The encoder has a contracting path with two consecutive convolutions followed by a max pooling operation for progressive downsampling, and the decoder has a symmetric expansive path for upsampling and reconstruction of the output segmented image (Ronneberger et al., 2015). The U-Net CNN architecture implemented in this study is presented in Fig. 2, which contains four convolution blocks (CB) in the encoder, and the expansive path in the decoder contains the corresponding four upsampling blocks (UpB). In each convolution block, two consecutive convolutions of 3 × 3 kernel size are applied to the input images. This is followed by downsampling of the convolved images and passing it to the next convolution block. The rectified linear unit (ReLU) activation function (Nair and Hinton, 2010) using the He initialization (He et al., 2015) was implemented after the convolution steps, to add nonlinearity to the model. Mathematically the ReLU activation function is expressed as:

$$f(x) = \begin{cases} 0, x < 0 \\ x, x \geq 0 \end{cases} \quad (1)$$

Downsampling is achieved by implementation of a 2 × 2 max pooling operation after each convolution block. The downsampling due to the convolutions on the images and feature maps in the convolution blocks is countered using the padding operation where the size of the images and feature maps is maintained by applying an even padding to the convolved and downsampled images. The number of feature maps obtained from convolutions is doubled at every downsampling block.

In the decoder branch, the upsampling is implemented using a 2 × 2 nearest neighbor interpolation. There is no training implemented in the decoder section. Hence no new weights are generated in the upsampling blocks. To retrieve spatial information lost during downsampling in the encoder branch and reconstruct the output image to its original size, skip connections are applied (Drozdzal et al., 2016). Our network uses four skip connections to concatenate the upsampled feature maps in the decoder branch with the corresponding convolution feature maps in the encoder branch. After upsampling and concatenation using skip connections, two convolution operations of kernel size 3 × 3 each, are implemented on the concatenated feature map. ReLU activation function is applied following the convolutions. Using the even padding operation, the feature map size is maintained constant at each upsampling block, however, the number of feature maps reduce to ¼th of the maps before the convolutions. The last upsampling block, UpB4, contains a final convolutional layer with a convolution operation of 1 × 1 kernel size, and a sigmoidal activation function that outputs a value between 0 and 1, which may be interpreted as a probability value. These 'probability values' are used for semantic segmentation of the image into objects (fracture-traces and background non-trace pixels, in the present case) as described below (Section 3.2.4). The output image thus created has the same dimensions as the input image.

3.2.3. U-NET CNN training

The training of the U-Net CNN was conducted for 100 epochs, with 300 training steps and 100 validation steps in each epoch. The training was monitored using the focal loss-based sigmoidal focal loss function (Lin et al., 2017) for both training and validation data. The sigmoidal focal loss function, FL (Eq. (3)), is derived from the cross-entropy loss function, CE (Eq. (2)) by addition of a balancing parameter, α, and a modulating parameter γ to the cross-entropy loss function. The CE loss function is expressed as:

$$CE(p_t) = -\log(p_t) \quad (2)$$

where, CE = Cross entropy loss, and p_t is the predicted probability.

Adding the balancing and modulating factors α and γ, respectively, the focal loss function, FL, is expressed as:

$$FL(p_t) = -\alpha_t(1-p_t)^{\gamma}\log(p_t) \quad (3)$$

$$\text{where, } \alpha_t = \begin{cases} \alpha, y = 1 \\ 1-\alpha, otherwise \end{cases} \quad (4)$$

such that, for this study, $\alpha = 0.25$, $\gamma = 2.0$, and y = ground truth class value.

The sigmoidal focal loss function was introduced by Lin et al. (2017) to optimize the loss for datasets with imbalance between the background class and other classes. By introducing the weight factor $-\alpha_t(1-p_t)^{\gamma}$ to the CE function, the FL function down-weights the loss of easy-to-classify background samples and amplifies the loss for the misclassified samples. Hence, the FL function focusses on misclassified positives, and reduces the bias introduced by the accurate classification of the background non-trace pixels. The loss function was optimized using the root mean squared propagation (RMSprop) optimizer (Hinton et al., 2012; Tieleman and Hinton 2012; see also Fan et al., 2022). Optimizers are used to update the weights and adjust the learning rates during each epoch while minimizing the loss function and improving the overall accuracy. The RMSprop optimization algorithm is an extension of the stochastic gradient descent and momentum optimizers. It also

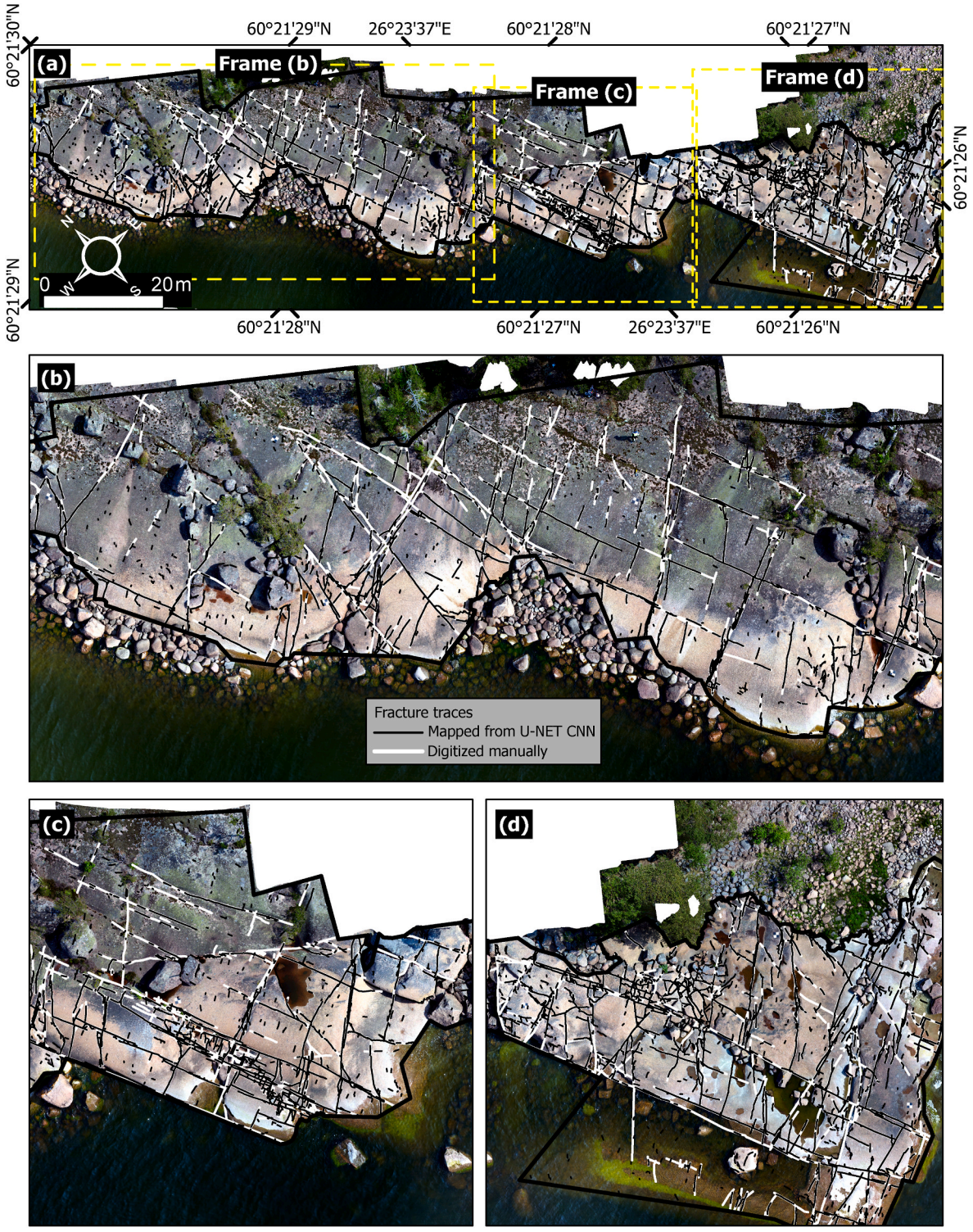

Fig. 6. Bedrock-fracture traces for the KB3 outcrop.

forms a backbone for the widely used ADAM optimizer. Being a stochastic mini-batch algorithm, the RMSprop optimizer uses an adaptive learning rate for optimizing the loss. It calculates the gradient of the loss function with respect to the model weights and updates the weights in the opposite direction of the gradient to minimize the loss (Eq. (5)). Additionally, the learning rate for each weights parameter is scaled using the moving average of the squared gradients (Eq. (6)). This prevents the directional oscillations of the loss and hence stabilizes the gradient and optimization trajectory. The RMSprop optimizer is mathematically expressed as:

$$E\left[g^2\right](t) = \beta E\left[g^2\right](t-1) + (1-\beta)\left(\frac{\partial c}{\partial w}\right)^2 \tag{5}$$

where E [g] is the moving average of squared gradients,

β is hyperparameter that controls the decay rate of the moving average of the squared gradients, and

$\frac{\partial c}{\partial w}$ is gradient of the cost function with respect to the weight w;

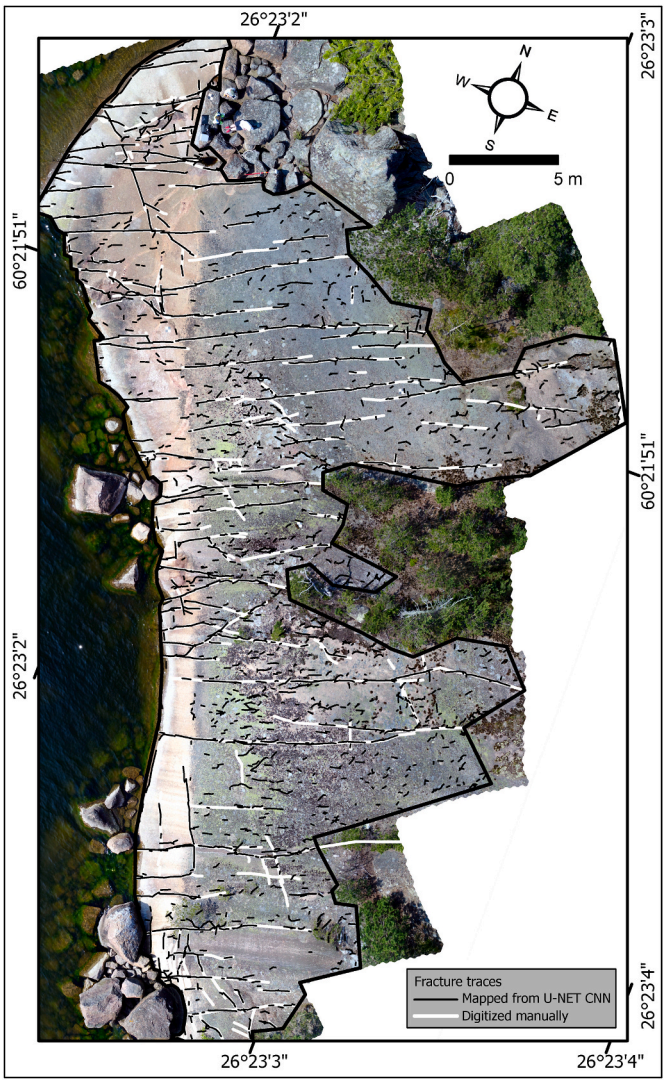

Fig. 7. Bedrock-fracture traces for the KB7 outcrop.

Accordingly, the weights for consecutive neurons are updated as follows:

$$w_{ij}(t) = w_{ij}(t-1) - \frac{\eta}{\sqrt{E[g^2]}} \frac{\partial c}{\partial w_{ij}} \tag{6}$$

where w_{ij} is the weight from neuron i to neuron j, and

η is the learning rate that controls the step size of the update.

Finally, the model was saved based on the optimal validation loss minimized by the sigmoidal focal loss function. The loss function for training and validation data at each epoch is presented in Fig. 3. The loss function for the validation set was optimal at epoch 32, while for the training data the optimization continues, implying overfitting of the model in the subsequent training epochs. An early stopping callback (Chollet and &, 2015) was used to prevent overfitting of the network. It stopped the training after epoch 32 as no improvement was observed in the validation loss function.

3.2.4. Postprocessing

The output of the U-Net are probability values for each pixel belonging to the fracture traces class (Step iiia). In Step iii(b), the ridge detection algorithm (Steger, 1998), available from (Lusnig, 2020), was used to identify and demarcate fracture-traces pixels, while the rest of the pixels were demarcated as background non-trace pixels. The ridge detection algorithm is less susceptible to background noise when applied to the images obtained from U-Net based segmentation. The method implements a Gaussian smoothing kernel, followed by scale-space analysis and calculating differential geometric properties to accurately model the fracture trace networks as linear-to-curvilinear features (Steger, 1998). Hence this step enables mapping of actual lines, line crossings and traces networks from predictions of the U-Net CNN. Next in steps iii c-e, the fracture pixels were vectorized as polylines and postprocessed to clean up the vectors.

3.2.5. Assessment of accuracy and geometric validations

The overall accuracy metrics of all the orthomosaics after vectorization, individual site-wise as well as training-, validation- and demonstration (test)-subset-wise are reported in Table 2. The trained model was used to implement fracture-trace prediction on the demonstration (test) site OG1 (Fig. 1j). This image and the corresponding traces were not used in the training or validation steps. Hence the results mapped for the OG1 orthomosaic are indicative of the real-world application of using a trained network for automated mapping of fracture traces from UAV-acquired images of the same spatial resolution as that on which the network is trained.

Additionally, for fracture trace data validation and analysis, the geometric intensity, orientations, and lengths of the automatically generated traces were compared to the manually digitized traces using visualizations and analyses provided by the Python package, fractopo (Ovaskainen, 2023). The intensity of fracturing within a target area is calculated from fracture traces by determining total ($\sum L$) and mean (L_C) length, trace count and the total area (A) within the target area boundary. Based on these geometric characteristics the *Fracture Intensity P21*

$$P21 = \frac{\sum L}{A} \tag{7}$$

and *Fracture Intensity P22*

$$P22 = P21 \times L_C \tag{8}$$

-parameters were calculated (Sanderson and Nixon, 2015; Dershowitz and Einstein, 1988). The orientations of fracture traces were compared by visually inspecting differences in length-weighted equal-area rose plots (Sanderson and Peacock, 2020), specifically focusing on the possible differences between dominant orientations. To compare the length distributions between the automatically mapped fracture traces and the manually mapped fracture-traces data, the length data of each trace dataset was plotted on a log-log scatter plot where complementary cumulative number is displayed as a function of fracture trace length (Bonnet et al., 2001). Furthermore, a power-law fit to the scatter data with the powerlaw Python package (Alstott et al., 2014), was used to quantify the differences between the length distributions of automatically- and manually-mapped fracture traces data. There is physical rationale for natural fracture lengths to follow a power-law but lognormal and exponential laws are also found to fit distributions of fracture lengths (Bonnet et al., 2001). A lognormal distribution of fracture lengths could be the result of e.g., stratabound fracture growth conditions (Odling et al., 1999).

4. Results

Figs. 4–10 present the fracture traces mapped from the trained network for each area in the training and validation set. Fig. 11 shows the traces mapped on the demonstration (test) site – OG1 area. The accuracy assessment metrics are presented in Table 2. The overall training accuracy is 99.41% and validation accuracy is 98.40%. For the demonstration (test) site OG1 the overall observed accuracy is 98.70%. The overall accuracy measures the accuracy of classification with respect to the 'trace'-pixels as well as 'non-trace'-pixels. Because of the

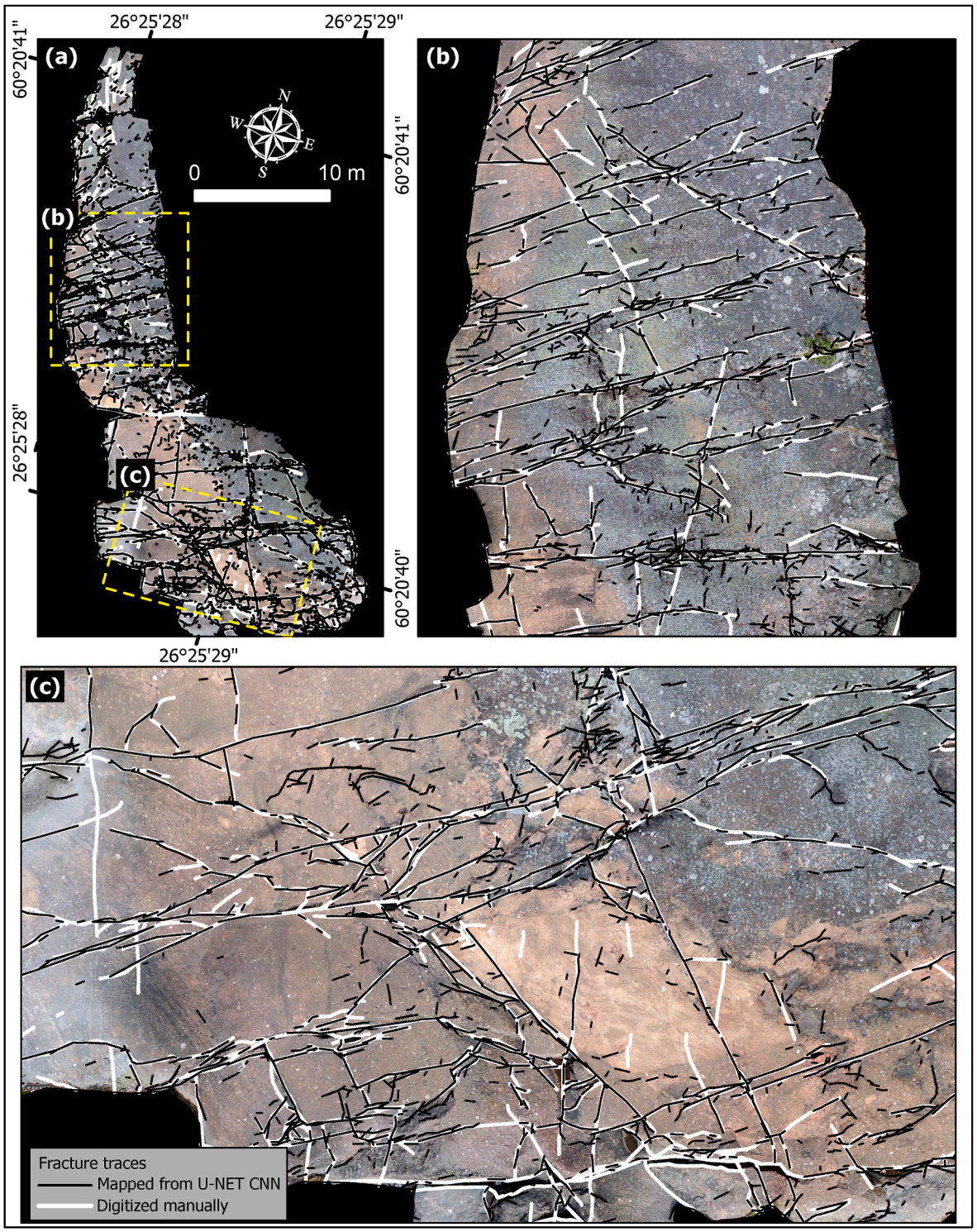

Fig. 8. Bedrock-fracture traces for the KL2_1 outcrop.

imbalanced training data, we report additional accuracy assessment metrics, viz., recall (true positive rate), Cohen's kappa coefficient, F1 scores and MIoU (mean of intersection of union) values to evaluate the traces-prediction efficiency of the trained model. The overall recall is 0.89, with kappa coefficient of 0.852, F1 score of 0.854 and the MIoU is 0.871. The error of omission of traces is 11.21%. The recall, kappa coefficient, F1 scores and MIoU for the validation sites are 0.802, 0.820, 0.829 and 0.845, respectively. The demonstration (test) site OG1 has recall, kappa coefficient, F1 scores and MIoU values of 0.752, 0.774 0.780 and 0.813, respectively. Figs. 12–17, show a comparison between the orientation-frequencies and the length distributions (Table 3) of the automatically mapped traces and manually mapped traces for the training, validation and testing sites respectively.

5. Discussion

The bedrock outcrops are rarely completely free of surface cover. Vegetation, bushes, moss, lichens, boulders, quaternary sediments,

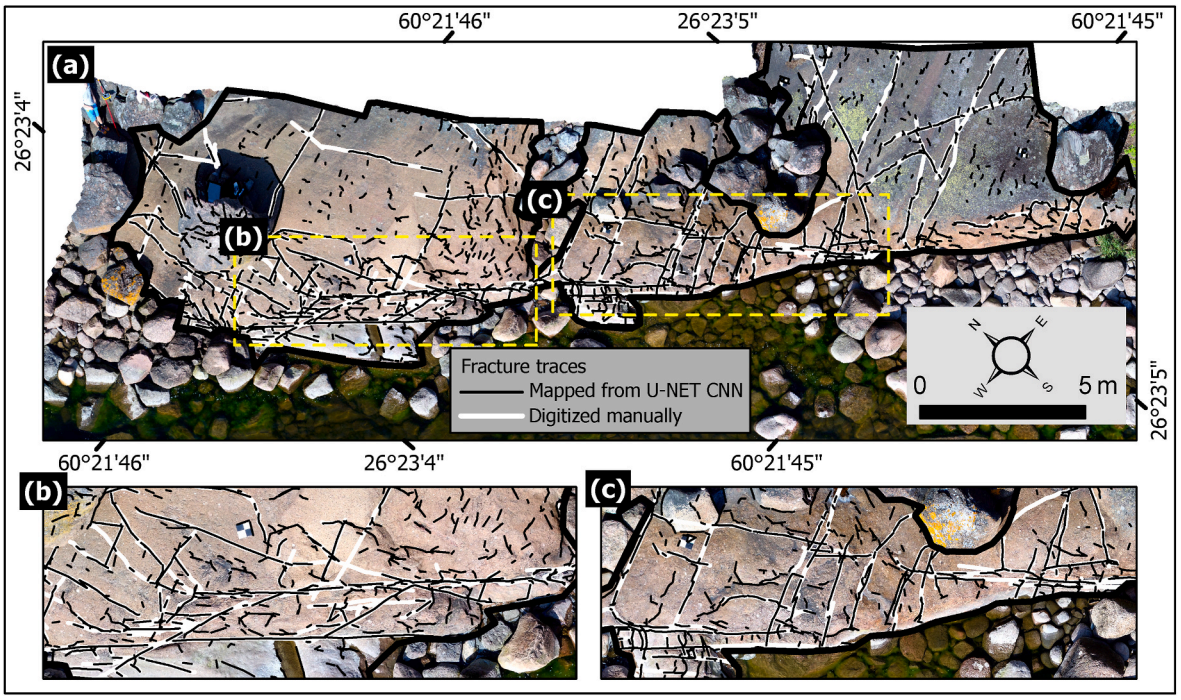

Fig. 9. Bedrock-fracture traces for the KB9 outcrop.

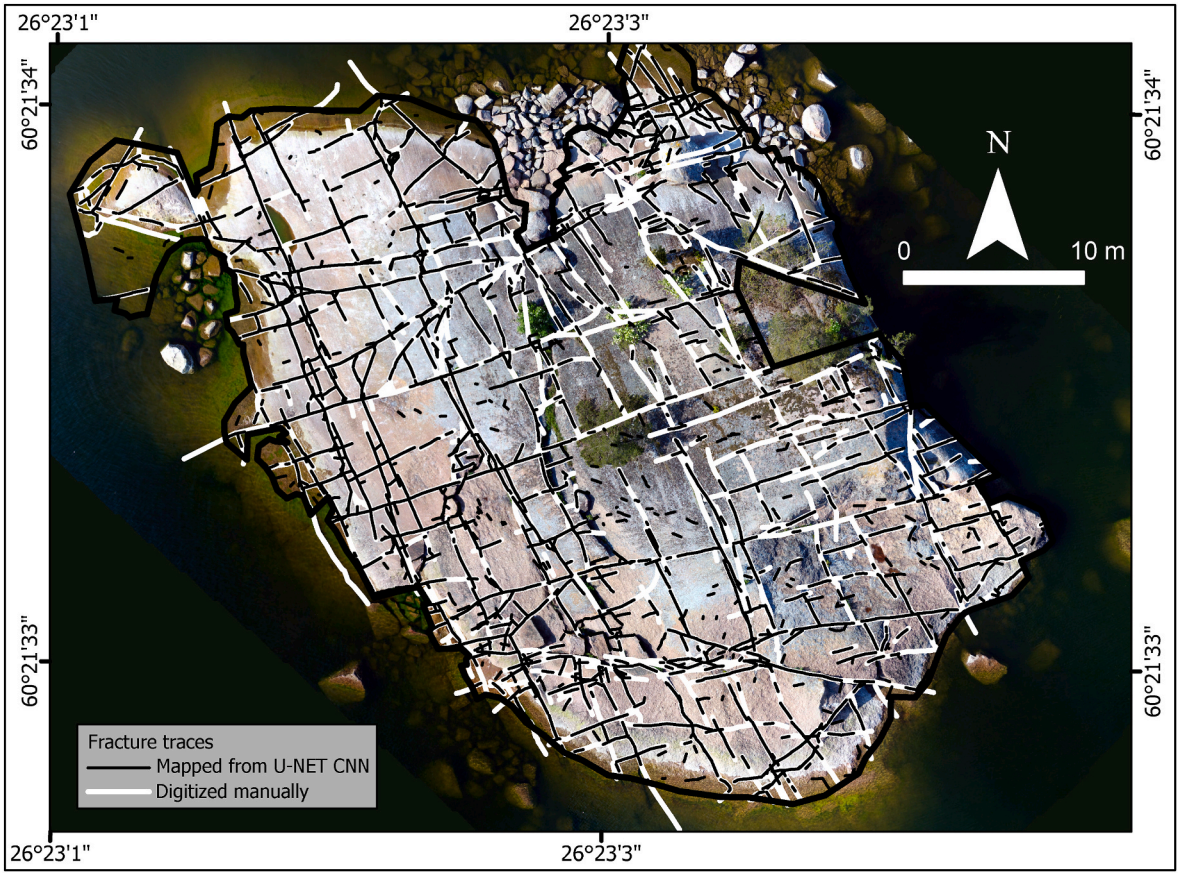

Fig. 10. Bedrock-fracture traces for the KB11 outcrop.

glacially reworked sediments, and even anthropogenic objects contribute to background noise and therefore obstruct detection of fracture traces from aerial imagery (Rohrbaugh et al., 2002; Ovaskainen et al., 2022; Zeeb et al., 2013). Additionally, variations in illumination and viewing geometry also affect the accurate demarcation of faults and fractures. Gradient-based edge detectors fail to differentiate between the

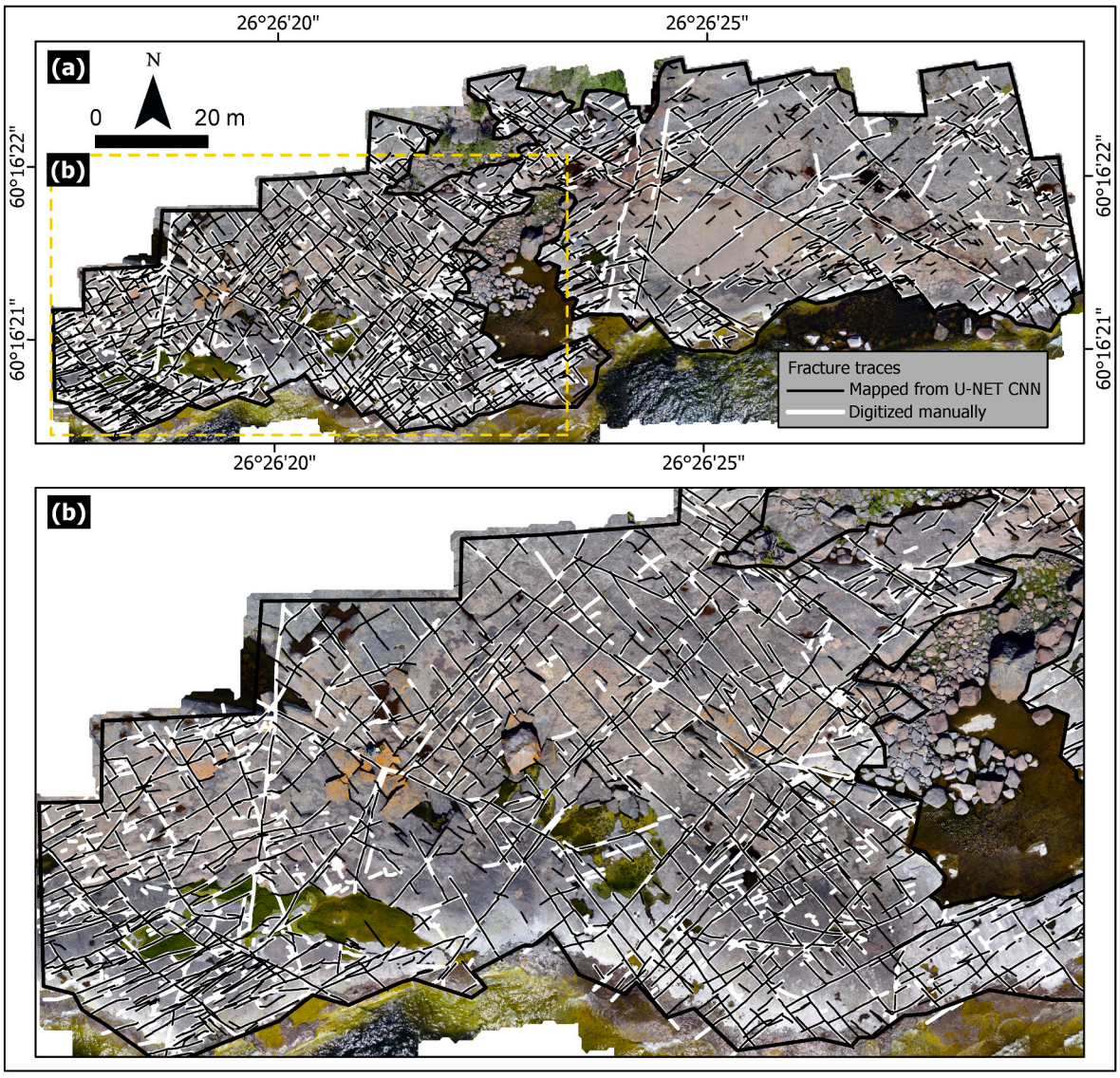

Fig. 11. Bedrock-fracture traces for the OG1 outcrop.

edges of the background objects and the actual traces of faults and fractures. Pre-processing methods such as gaussian smoothening are often applied to reduce the effects of background noise. However, when applied to bedrock images of the study area, e.g., Laplacian of Gaussian, the non-fracture-trace edges are not suppressed successfully (Chudasama et al., 2022). Hence, the conventional image processing methods such as edge detection result in high false positive rates. For shallow-learning-based machine learning methods, the surface cover types can be explicitly stated as different classes or masked in the training data. However, considering the diversity of the background objects and consequent censoring of fracture-related data, it leads to extensive manual identifications of the background classes and learning of low-level attributes of the corresponding features. Additionally, even for training machine learning models, the images must be processed using the pre-defined edge-detection filters, along multiple directions, over various scales. Therefore, real-world application of machine learning-based end-to-end automated mapping of bedrock fracture traces has until recently remained challenging.

However, deep learning-based methods are emerging to overcome the issues that impede the success of traditional methods. Several studies have demonstrated that the performance of CNN-based models for mapping faults and fracture traces is gradually improving (e.g.: Byun et al., 2021; Chen et al., 2021; Junior et al., 2021; Mattéo et al., 2021 and this study). For instance, Mattéo et al. (2021) is one of the few seminal studies that present a comprehensive application of CNNs for automatic mapping of faults from field-based optical photographs and topographic data. The study demonstrated the successful training and application of a U-Net CNN and assessed the model efficiencies using Tversky index (Tversky, 1977), that is a variant of the intersection over union metric (Jaccard, 1912; Tanimoto, 1958). The study also compared the false positive rate to the true positive rate using the receiving operating characteristic (ROC) curve (Fawcett, 2006). Additionally, the qualitative analysis of their results included extensive comparison of the density, azimuth and length distributions of the ground truth and the CNN predictions. A recent study by Kanoun et al. (2022) further builds from study by Mattéo et al. (2021) and reports comparable results with similar TI values. Another study by Byun et al. (2021) on rock fracture image segmentation has recall (true positive) rates of 0.643 and 0.614. The metrics used in previous studies are varied, both qualitatively and quantitatively, hence we are unable to present a direct comparison with the results presented in this study. However, Table 2 summarizes the results of commonly used evaluation metrics for this study.

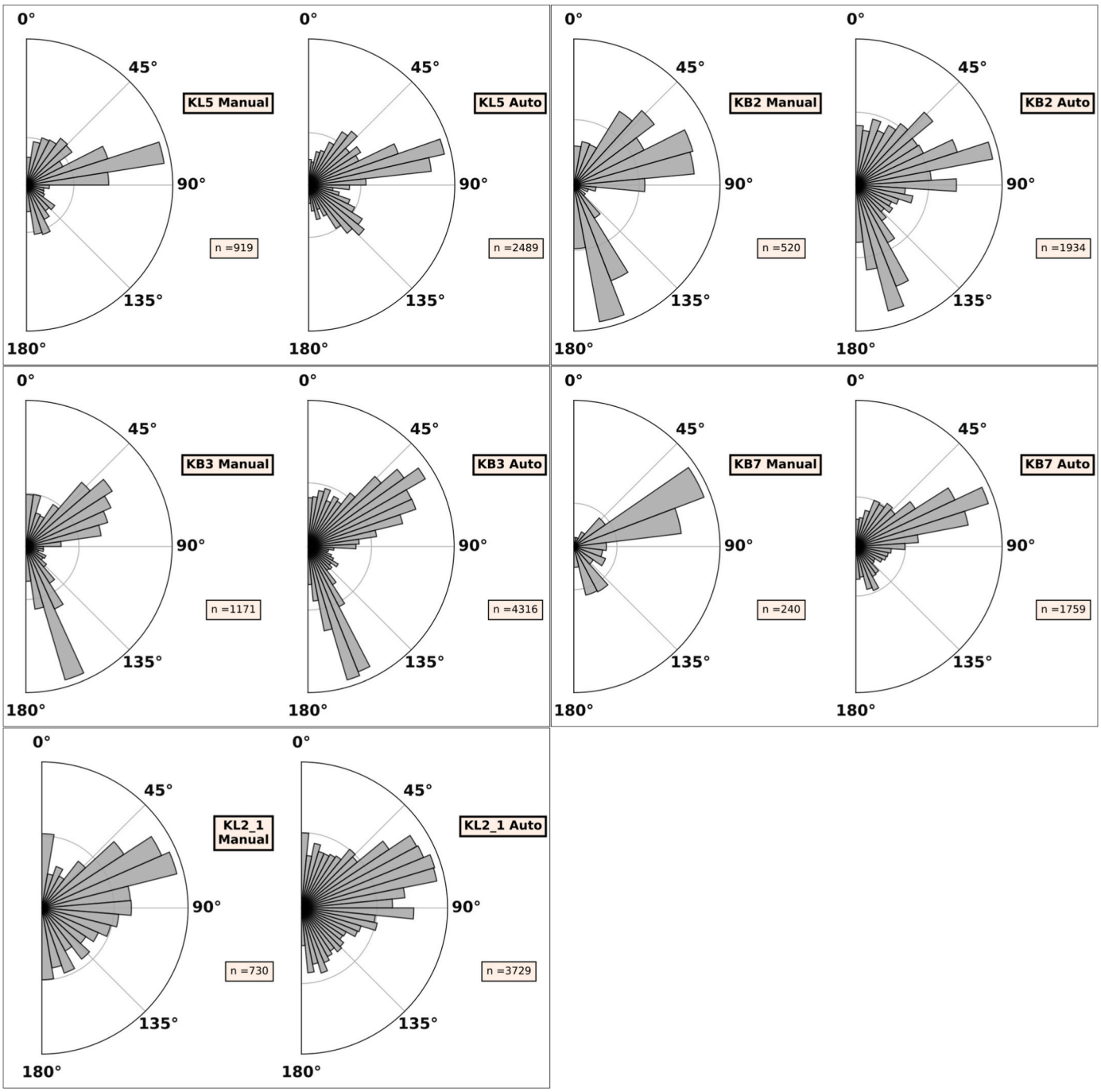

Fig. 12. Comparison of orientations between manually digitized and automatically predicted fracture traces of training sites using equal-area length-weighted rose plots.

5.1. Assessments of accuracies and performance

Since the vectorization of the traces was implemented after the training of the U-Net models (Section 3.2), and all the accuracy assessments are based on the comparisons of the U-Net-based automatically traced fractures with manually traced fractures, the accuracy metrics were reassessed after processing all orthomosaics through the trained U-Net. The results for all orthomosaics are reported individual site-wise as well as training-, validation- and demonstration-subset-wise metrics (Table 2).

The bedrock-fracture traces comprise only 1.5% of pixels in the training dataset, and hence the training dataset is highly imbalanced and biased towards the background non-trace class. Hence, in addition to overall accuracy, we also use other metrics that assess the performance of the U-Net in predicting the fracture-trace class. In this regard, True Positive Rate, TPR (recall) and error of omission are better indicators of the performance of the model. We also use a balanced accuracy score, which is the average of sensitivity and specificity (Table 2), (Urbanowicz and Moore, 2015) as an indicator of the efficiency of the model. Finally, the Cohen's kappa coefficient, F1 and the MIoU scores also provide holistic evaluations of the results. All results indicate high level of performance showing overall high recall values, Cohen's kappa coefficient, F1 and MIoU scores for both training-validation sites and the demonstration (test) site (Table 2).

Collective assessment of recall (TPR) and precision values can impart confidence to the trace mapping capabilities of the model. For instance,

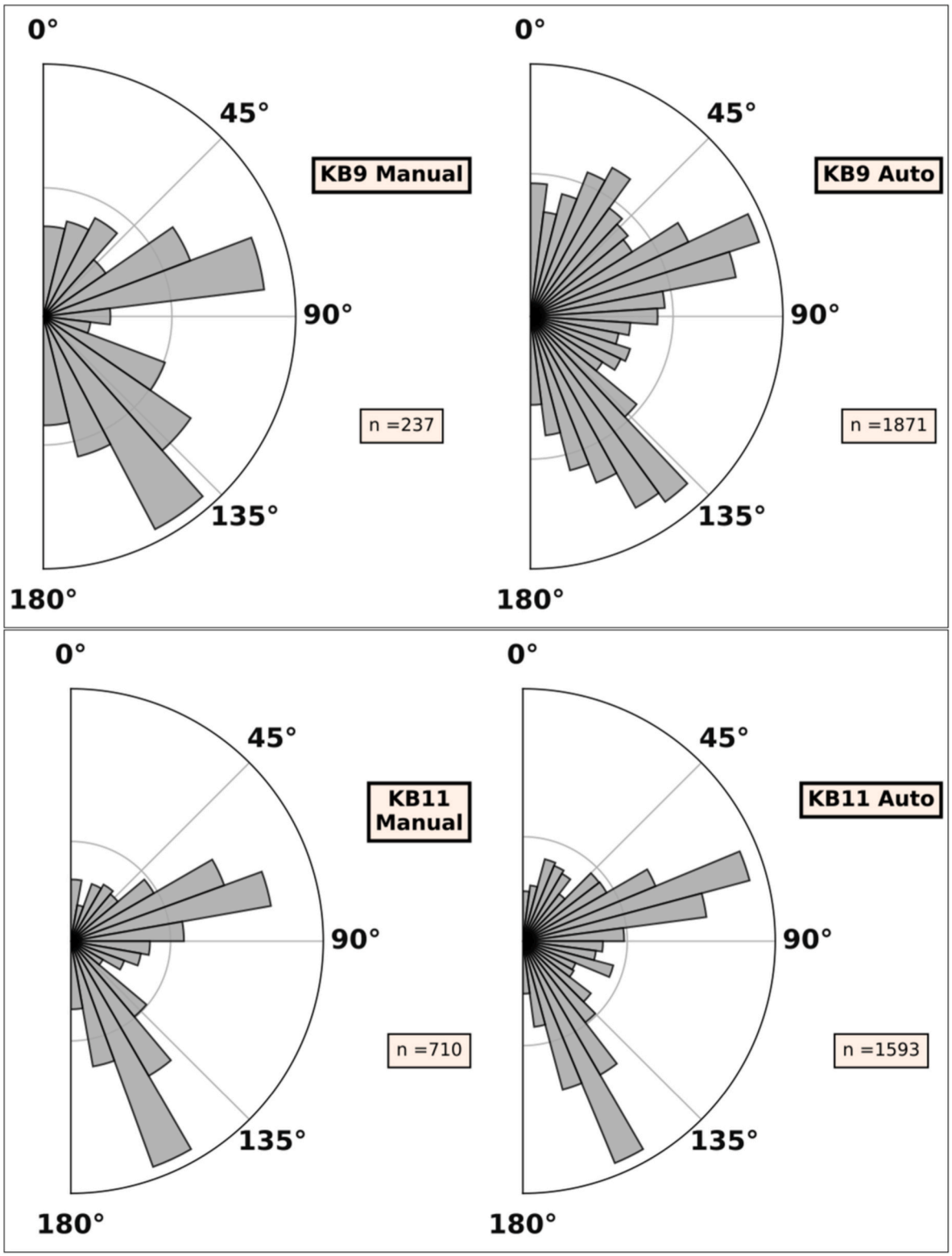

Fig. 13. Comparison of orientations between manually digitized and automatically predicted fracture traces of validation sites using equal-area length-weighted rose plots.

areas with high recall and high precision imply that the network has correctly identified high number of bedrock fracture trace pixels at high confidence (e.g., KB3 and KL2_1). Training site KB3 has recall 0.903 and precision 0.858, and training site KL2_1 has recall 0.964 and precision 0.890. However, high recall and low precision implies that the proportion of false positives in the results is high and hence the confidence in the results is low (e.g., KB2, KB7, KB9). Training sites KB2 and KB7 and validation site KB9 have recall values 0.946, 0.898 and 0.992 respectively, however, their corresponding precision values are 0.772, 0.621 and 0.651 respectively; of which site KB7 has the lowest performance. Low recall and high precision, on the contrary, would imply that although the error of omission of traces is high, the confidence in the

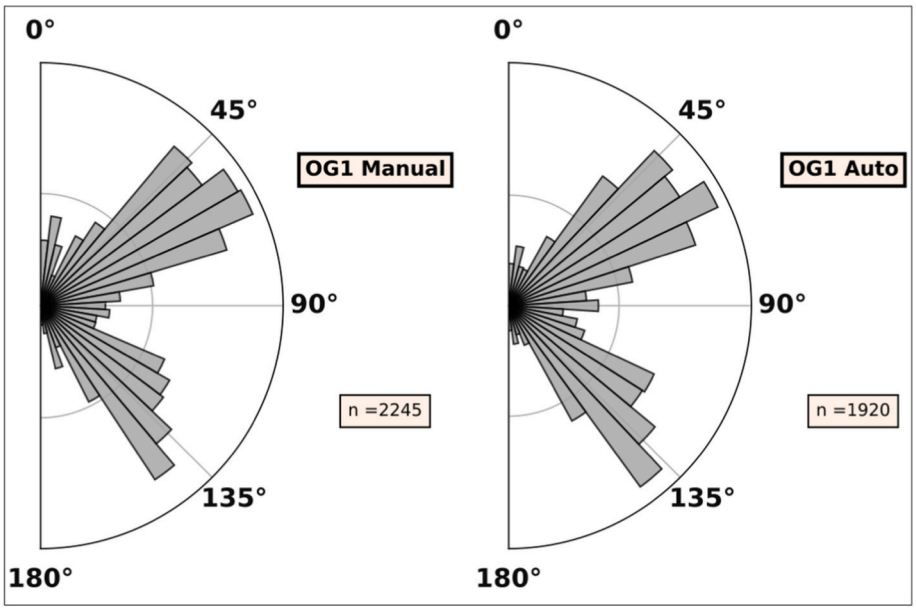

Fig. 14. Comparison of orientations between manually digitized and automatically predicted fracture traces of demonstration (test) site OG1 using equal-area length-weighted rose plots.

results is high because the relative proportion of false positives is less (e.g.: KB11 and OG1). Validation site KB11 has recall rate 0.771 but with a high precision value, 0.918. For the demonstration (test) site OG1 the recall rate is 0.752 but precision value is 0.811, indicating high confidence in the results. Quantitatively, for training datasets the recall and precision values are 0.920 and 0.810, respectively; for the validation sites these are 0.802 and 0.858, respectively, and the overall recall and precision for the entire training and validation set is 0.890 and 0.820, respectively.

In summary, the U-Net-based workflow presented in this study performs well in identification and demarcation of fractures from UAV-acquired orthophotographs. It outperforms the current state-of-the-art accuracies, for instance, those reported by Byun et al. (2021).

Furthermore, theoretically, given adequate training data, deep learning-based models are likely to be able to inherently distinguish between the desired classes and the background noise. This is because CNNs are capable of learning spatial relationships of pixel through the hierarchical convolutional approach. To test this hypothesis, we provided to the network images from sites that contained the background noise, which often is the case in real-world datasets. Training site KL2_1, for example, has dense moss and lichen cover on the outcrop (Fig. 8b), and despite this background noise, the traces predictions show true positive rate of 0.964 for this site with precision of 0.890. The kappa coefficient and F1 scores are 0.922 and 0.926 respectively, further validating the noise suppression capabilities of the model.

This study demonstrates that state-of-the-art deep learning methods are useful to overcome some of the challenges encountered by the conventional semi-automatic and automatic edge-detection method for mapping fault and fracture traces. The success of CNNs can be attributed to the capabilities of CNNs to extract features hierarchically employing multi-scale convolutional kernels. The network can be trained to identify multidirectional kernels at each level of convolution, thus learning specific spatial hierarchies. The contracting path facilitates downsampling of spatial resolutions and hence was able to learn progressively larger and prominent fracture traces. Progressive convolution facilitates extraction of progressively higher level features, and hence a CNN can adaptively learn spatial hierarchies of features from low-to high-level patterns. A U-Net model architecture in particular is suited to these tasks because the contracting path captures the spatial context and a symmetric expanding path facilitates relocalization of features (Ronneberger et al., 2015). The U-Net and seg-net are the most frequently used CNNs for mapping fracture traces (Marques et al., 2022; Qiao et al., 2021); and these studies also indicate that U-Net excels in terms of performance metrics.

5.2. Geometric comparisons of results

In terms of orientation distributions, (Figs. 12–14), the orientations of the automatically mapped traces resemble the manually digitized traces for all target areas, with similar orientation maxima. Consequently, automatic trace mapping, as demonstrated in this paper, is amenable to interpretation of major fracture patterns and stress orientations in a given area. The geological interpretations of the results, at least in terms of orientation, are equivalent to past studies done in the area using the manually mapped fractures (Ovaskainen, 2020; Skyttä et al., 2021).

Nonetheless, fragmentation of fracture traces is a limitation to this approach. For instance, for all areas, the automatic trace generation results in two-to-six times more number of fracture traces than the manually digitized ones (Table 3). As a result, the mean length of the automatically generated traces is proportionately lower (Table 3). Consequently, *Fracture Intensity P21* values also vary to some extent from one site to another site when comparing the results of automated tracing to manual tracing (Table 3). In general, the lower *Dimensionless Intensity P22* values for the automatically mapped fracture traces is a result of comparatively lower values of mean trace length for automatically mapped fracture traces results (Table 3).

The fragmentation also affects the distributions of the lengths of the automatically mapped fracture-traces and results in deviations from the distributions of the lengths of the manually digitized fracture traces (Figs. 15-17), because of which different cut-off thresholds had to be used for defining the automatically mapped and manually digitized fracture traces. For instance, the cut-off values used for the automatically mapped fracture traces for KB2 and KB7 were 0.3 m and 0.22 m, respectively; while the cutoff values for the manually digitized fracture traces were 7.15 m and 4.21 m, respectively. Similarly, the power-law exponents determined for KB2 and KB7 are −1.097 and −1.277 for the automatically mapped fracture traces, respectively; and −3.578 and −2.779 respectively, for the manually mapped fracture traces. For other areas also similar types of differences are observed. Because the

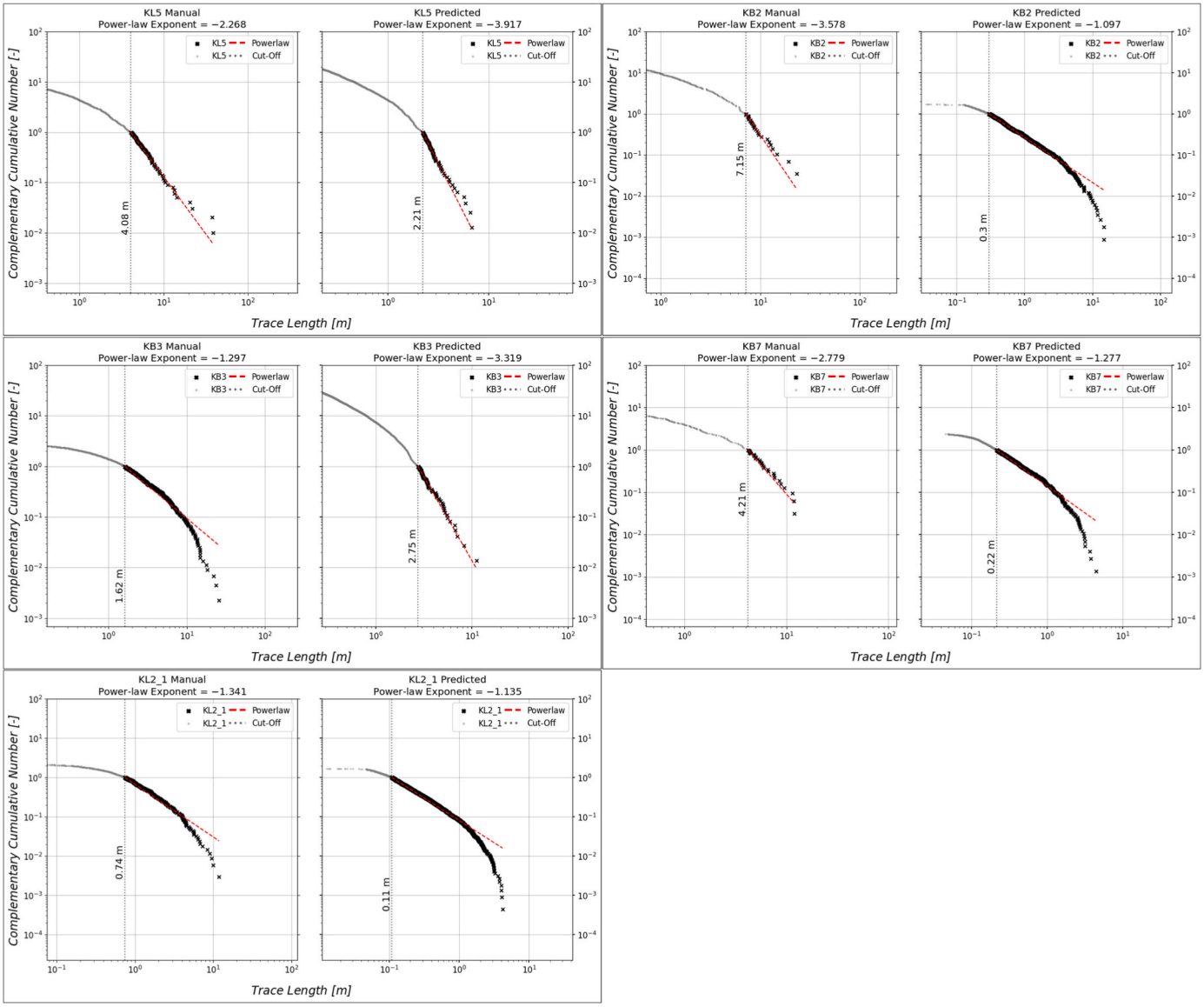

Fig. 15. Comparison of length distributions between manually digitized and automatically predicted fracture traces of training sites using plots with complementary cumulative number as a function of fracture trace length. Both x- and y-axis are logarithmic. Power-law fits to the truncated length data are displayed. The length data is truncated by an indicated cut-off value that is automatically determined for the purpose of fitting the power-law.

accuracy metrics indicate a strong correlation between the automatically and manually mapped fracture traces, these differences in length distribution are a result of suboptimal vectorization process and needs further improvement.

6. Conclusions and future work

The U-Net CNN workflow used in this paper effectively identifies and maps fracture traces from the Rapakivi granites in Loviisa with high accuracy metrics. Furthermore, the geometric properties and topological properties of the automatically traced fractures are comparable to the manually mapped fracture traces. This U-Net based workflow can be effectively adapted and used for automatic detection and mapping of fracture traces from airborne orthorectified photographs in other areas. The initial investment of resources in manual mapping and digitization of accurate, and topologically valid fracture traces from UAV-acquired images from some parts of the area of interest can be used to generate training data that can then be used for cost-effective, and rapid mapping of fracture traces in other parts of the area.

However, the workflow used in this study is not an end-to-end automation workflow, as it requires significant data pre-processing and training data preparation, which requires human intervention. Future research will focus on attempting to automate some of these procedures. Furthermore, CNNs are hierarchical learning algorithms that learn features at multiple scales. However, transfer learning across images of different resolutions is not possible with the U-Net architecture used in this study. More research needs to be conducted in developing CNN architectures capable of transfer learning. Additionally, in automated fracture traces mapping, similar to most machine learning applications, the class of interest is the minority class and the training data are highly imbalanced and biased towards the majority class. Conventional algorithms developed for addressing this issue using shallow learning algorithms are not likely to perform well for CNNs. Future work will be focused on addressing this issue, particularly in the context of tracing fractures from aerial photographs. Finally, the present work is limited to mapping fractures from the aerial photographs only. The algorithm can be improvised to application to automated tracing of other important linear or curvilinear geological features from different

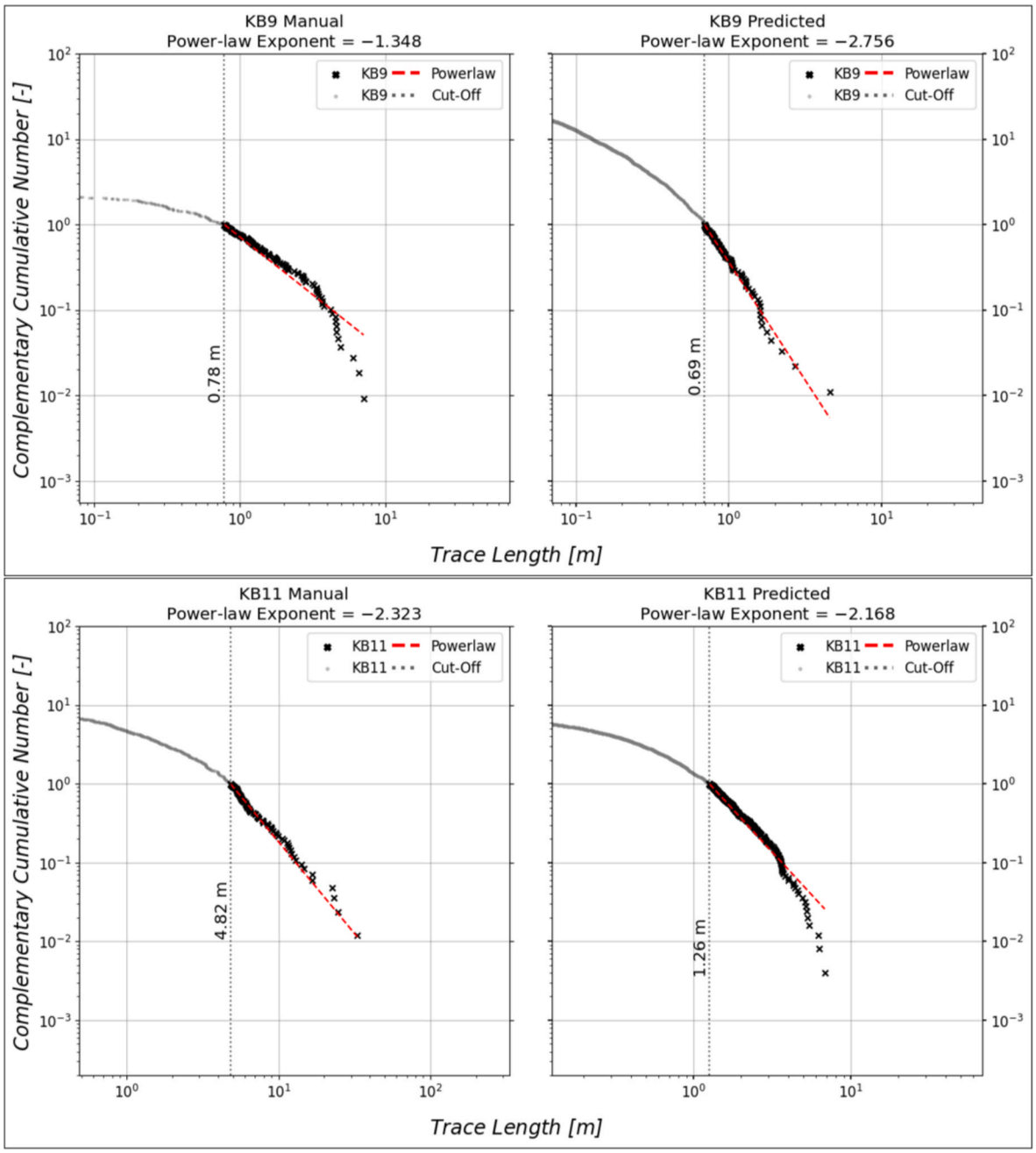

Fig. 16. Comparison of length distributions between manually digitized and automatically predicted fracture traces of validation sites. See Fig. 15 caption for plotting method synopsis.

images such as remote sensing, airborne magnetics and gravity images (Engström et al., 2023; Nordbäck et al., 2023; Vasuki et al., 2014; Kovesi, 1997, 1999).

Authorship statement

Bijal Chudasama (corresponding author): Conceptualization, inputs to code, technical testing, data pre-processing, implementation, model accuracy assessments, analysis, interpretations, writing. Nikolas Ovaskainen: Conceptualization, data preparation, code improvement, optimization and technical testing, topological network analysis, interpretations, and writing. Jonne Tamminen: Conceptualization, code development (main coder) and technical testing. Jon Engström, Nordbäck Nicklas, Ismo Aaltonen: Conceptualization, review, edits, feedback and supervision, project management, funding acquisition.

Code availability

Name of the code: ALSA - Automatic Fracture Trace Extraction.
Contact: Nikolas Ovaskainen (GTK): nikolas.ovaskainen@gtk.fi.
Program language: Python.
The source codes are available for downloading at the link: https://github.com/nialov/ALSA (latest version) and https://github.com/JonneTyo/ALSA (version used in Tamminen, 2020).

Declaration of competing interest

The authors declare that they have no known competing financial interests or personal relationships that could have appeared to influence the work reported in this paper.

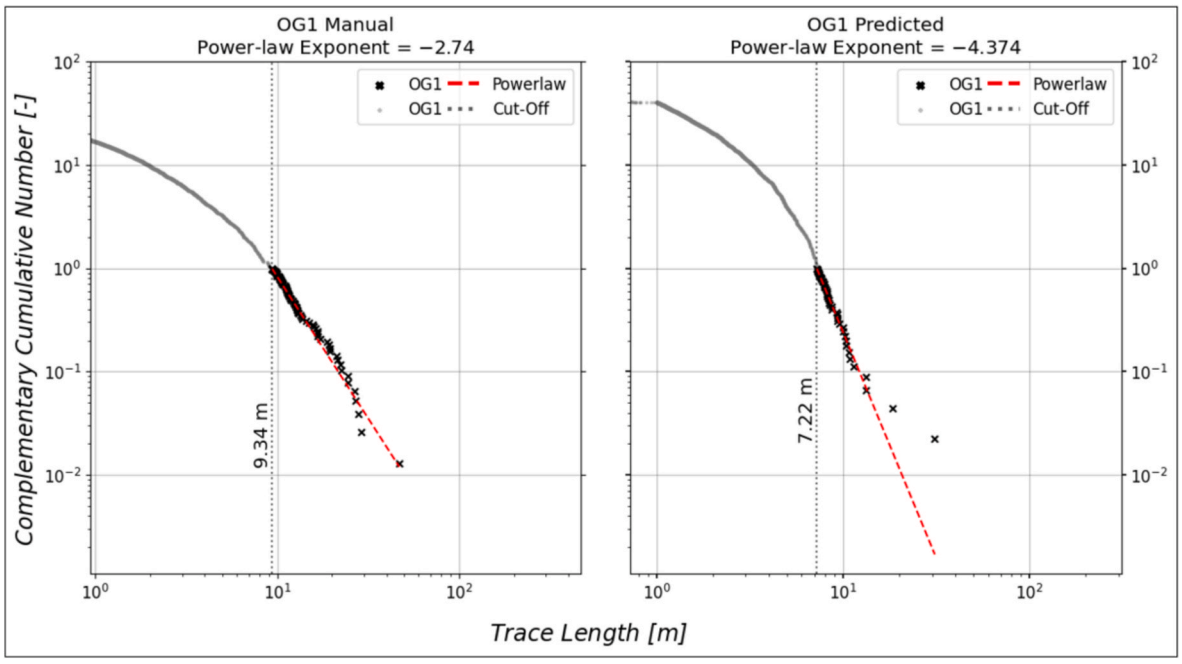

Fig. 17. Comparison of length distributions between manually digitized and automatically predicted fracture traces of demonstration (test) site OG1. See Fig. 15 caption for plotting method synopsis.

Table 3
Comparison of geometric parameters between manual and predicted trace networks.

Traces	Area [m^2]	Number of Traces	Trace Max Length [m]	Trace Mean Length [m]	Fracture Intensity P21 [m/m^2]	Dimensionless Intensity P22 [-]
KL5 Auto	1105.73	2489	6.84	0.5	1.13	0.56
KL5 Manual	1105.73	919	38.59	1.76	1.46	2.57
KB2 Auto	1671.06	1934	14.66	0.76	0.88	0.68
KB2 Manual	1671.06	520	23.28	2.04	0.63	1.29
KB3 Auto	3651.41	4316	11.13	0.5	0.59	0.29
KB3 Manual	3651.41	1171	25.73	2.07	0.66	1.38
KB7 Auto	534.68	1759	4.44	0.33	1.1	0.37
KB7 Manual	534.68	240	11.94	1.9	0.85	1.63
KL2_1 Auto	418.55	3729	4.18	0.26	2.34	0.61
KL2_1 Manual	418.55	730	11.9	1.11	1.93	2.13
KB9 Auto	163.77	1871	4.59	0.21	2.42	0.51
KB9 Manual	163.77	237	7.1	1.1	1.59	1.76
KB11 Auto	1237.9	1593	6.82	0.71	0.92	0.65
KB11 Manual	1237.9	710	33.11	2.2	1.26	2.78
OG1 Auto	7001.56	1920	31.02	2.5	0.69	1.72
OG1 Manual	7001.56	2245	46.93	2.25	0.72	1.63

Data availability

All the data used for this study and created in this study are released online as follows:-

UAV-acquired orthomosaics of Loviisa shoreline outcrops: Nordbäck and Ovaskainen (2022)

Manually mapped traces from UAV-acquired images of Loviisa shoreline outcrops: Ovaskainen and Nordbäck (2022)

Automatically mapped traces from UAV-acquired images of Loviisa shoreline outcrops: Chudasama and Ovaskainen (2022a)

Weights for automatic two-dimensional bedrock fracture trace mapping from outcrop images: Chudasama and Ovaskainen (2022b)

Acknowledgements

This study was funded by Kallioperän rikkonaisuus – Bedrock fracturing project at the Geological Survey of Finland (50402-20101). We also acknowledge the Finnish Research Programme on Spent Fuel Management (2019–2022) and Geological Survey of Finland for funding the KYT KARIKKO -project which provided the drone orthomosaics and manually digitized traces. Insightful comments and suggestions from two anonymous reviewers and the handling editor are truly appreciated. These have led to significant improvement of the manuscript.

References

Abdullah, A., Akhir, J.M., Abdullah, I., 2010. Automatic mapping of lineaments using shaded relief images derived from digital elevation model (DEMs) in the Mara– -sungi Lembing area, Malaysia. Electron. J. Geotech. Eng. 15 (J), 1–9.

Aghaee, A., Shamsipour, P., Hood, S., Haugaard, R., 2021. A convolutional neural network for semi-automated lineament detection and vectorisation of remote sensing data using probabilistic clustering: a method and a challenge. Comput. Geosci. 151, 104724 https://doi.org/10.1016/j.cageo.2021.104724. March.

Alstott, J., Bullmore, E., Plenz, D., 2014. Powerlaw: a Python package for analysis of heavy-tailed distributions. PLoS One 9, e85777. https://doi.org/10.1371/journal.pone.0085777.

Araya-Polo, M., Dahlke, T., Frogner, C., Zhang, C., Poggio, T., Hohl, D., 2017. Automated fault detection without seismic processing. Lead. Edge 36 (3), 208–214. https://doi.org/10.1190/tle36030208.1.

Arun, P.V., Buddhiraju, K.M., 2016. A deep learning based spatial dependency modelling approach towards super-resolution. In: International Geoscience and Remote Sensing

Symposium (IGARSS), 2016-Novem, pp. 6533–6536. https://doi.org/10.1109/IGARSS.2016.7730707.
Arun, P.V., Herrmann, I., Budhiraju, K.M., Karnieli, A., 2019. Convolutional network architectures for super-resolution/sub-pixel mapping of drone-derived images. Pattern Recogn. 88, 431–446. https://doi.org/10.1016/j.patcog.2018.11.033.
Arun, P.V., Buddhiraju, K.M., Porwal, A., Chanussot, J., 2020. CNN based spectral super-resolution of remote sensing images. Signal Process. 169, 107394 https://doi.org/10.1016/j.sigpro.2019.107394.
Badrinarayanan, V., Kendall, A., Cipolla, R., 2017. Segnet: a deep convolutional encoder-decoder architecture for image segmentation. IEEE Trans. Pattern Anal. Mach. Intell. 39 (12), 2481–2495.
Bemis, S.P., Micklethwaite, S., Turner, D., James, M.R., Akciz, S., T. Thiele, S., Bangash, H.A., 2014. Ground-based and UAV-Based photogrammetry: a multi-scale, high-resolution mapping tool for structural geology and paleoseismology. J. Struct. Geol. 69 (PA), 163–178. https://doi.org/10.1016/j.jsg.2014.10.007.
Bond, C.E., Gibbs, A.D., Shipton, Z.K., Jones, S., 2007. What do you think this is? "Conceptual uncertainty" in geoscience interpretation. GSA Today (Geol. Soc. Am.) 17 (11), 4–10. https://doi.org/10.1130/GSAT01711A.1.
Bonetto, S., Facello, A., Umili, G., 2017. A new application of CurvaTool semi-automatic approach to qualitatively detect geological lineaments. Environ. Eng. Geosci. 23 (3), 179–190. https://doi.org/10.2113/gseegeosci.23.3.179.
Bonnet, E., Bour, O., Odling, N.E., Davy, P., Main, I., Cowie, P., Berkowitz, B., 2001. Scaling of fracture systems in geological media. Rev. Geophys. 39 (3), 347–383. https://doi.org/10.1029/1999RG000074.
Byun, H., Kim, J., Yoon, D., Kang, I.S., Song, J.J., 2021. A deep convolutional neural network for rock fracture image segmentation. Earth Science Informatics 14 (4), 1937–1951. https://doi.org/10.1007/s12145-021-00650-1.
Canny, J., 1986. A computational approach to edge detection. IEEE Trans. Pattern Anal. Mach. Intell. (6), 679–698.
Chen, J., Zhou, M., Huang, H., Zhang, D., Peng, Z., 2021. Automated extraction and evaluation of fracture trace maps from rock tunnel face images via deep learning. Int. J. Rock Mech. Min. Sci. 142, 104745 https://doi.org/10.1016/j.ijrmms.2021.104745. September 2020.
Cheng, Z., Yang, Q., Sheng, B., 2015. In: Deep Colorization. Proceedings of the IEEE International Conference on Computer Vision, 2015 Inter, pp. 415–423. https://doi.org/10.1109/ICCV.2015.55.
Cheng, J.Y., Chen, F., Alley, M.T., Pauly, J.M., Vasanawala, S.S., 2018. Highly Scalable Image Reconstruction Using Deep Neural Networks with Bandpass Filtering, pp. 1–9. http://arxiv.org/abs/1805.03300.
Chopra, S., Kumar, R., Marfurt, K.J., 2014. Seismic discontinuity attributes and Sobel filtering. October. In: 2014 SEG Annual Meeting. OnePetro.
Chudasama, B., Ovaskainen, N., 2022a. Automatically Mapped Traces from UAV-Acquired Images of Loviisa Shoreline Outcrops (1.0.0). https://doi.org/10.5281/zenodo.7077494 [Data set]. *Zenodo*.
Chudasama, B., Ovaskainen, N., 2022b. Weights for Automatic Two-Dimensional Bedrock Fracture Trace Mapping from Outcrop Images (1.0.0). https://doi.org/10.5281/zenodo.7077620 [Data set]. Zenodo.
Chudasama, B., Ovaskainen, N., Tamminen, J., 2022. S2304 U-NET Convolutional neural networks for automated mapping of bedrock fracture traces from UAV-acquired images. Aug.. In: The 21st Annual Conference of the International Association of Mathematical Geosciences, vol. 2022, pp. 326–327, 29 Aug. – 3 Sept. 2022. Nancy, France. Abstracts. https://www.iamgconferences.org/iamg2022/ShortAbstractsIAMG2022.pdf.
Dering, G.M., Micklethwaite, S., Thiele, S.T., Vollgger, S.A., Cruden, A.R., 2019. Review of drones, photogrammetry and emerging sensor technology for the study of dykes: best practises and future potential. J. Volcanol. Geoth. Res. 373, 148–166. https://doi.org/10.1016/j.jvolgeores.2019.01.018.
Dershowitz, W.S., Einstein, H.H., 1988. Characterizing rock joint geometry with joint system models. Rock Mech. Rock Eng. 21, 21–51. https://doi.org/10.1007/BF01019674.
Dollár, P., Zitnick, C.L., 2015. Fast edge detection using structured forests. IEEE Trans. Pattern Anal. Mach. Intell. 37 (8), 1558–1570. https://doi.org/10.1109/TPAMI.2014.2377715.
Drozdzal, M., Vorontsov, E., Chartrand, G., Kadoury, S., Pal, C., 2016. The importance of skip connections in biomedical image segmentation. In: International Workshop on Deep Learning in Medical Image Analysis, International Workshop on Large-Scale Annotation of Biomedical Data and Expert Label Synthesis. Springer, Cham, pp. 179–187.
Duda, R.O., Hart, P.E., 1972. Use of the Hough transformation to detect lines and curves in pictures. Commun. ACM 15 (1), 11–15. https://doi.org/10.1145/361237.361242.
Eliason, J.R., 1992. Mapping fractures remotely for earthquake hazard assessment by the use of topographic and seismic hypocenter data. Episodes 15, 75–82. https://doi.org/10.18814/epiiugs/1992/v15i1/012.
Engström, J., Markovaara-Koivisto, M., Ovaskainen, N., Nordbäck, N., Paananen, M., Aaltonen, I., Martinkauppi, A., Laxström, H., Wik, H., 2023. Aerogeophysics and Light Detecting and Ranging (LiDAR)-Based Lineament Interpretation of Finland at the Scale of 1:500 000, EGUsphere [preprint]. https://doi.org/10.5194/egusphere-2023-448, 2023.
Fan, S., Zhang, X., Song, Z., 2022. Imbalanced sample selection with deep reinforcement learning for fault diagnosis. IEEE Trans. Ind. Inf. 18 (4), 2518–2527. https://doi.org/10.1109/TII.2021.3100284.
Fawcett, T., 2006. An introduction to ROC analysis. Pattern Recogn. Lett. 27 (8), 861–874. https://doi.org/10.1016/j.patrec.2005.10.010.
Gautam, A., Sit, M., Demir, I., 2022. Realistic river image synthesis using deep generative adversarial networks. Frontiers in Water 4, 1–13. https://doi.org/10.3389/frwa.2022.784441.
Gong, M., Yang, H., Zhang, P., 2017. Feature learning and change feature classification based on deep learning for ternary change detection in SAR images. ISPRS J. Photogrammetry Remote Sens. 129, 212–225. https://doi.org/10.1016/j.isprsjprs.2017.05.001.
Guitton, A., 2018. 3D convolutional neural networks for fault interpretation. June. In: 80th EAGE Conference and Exhibition 2018, vol. 2018. European Association of Geoscientists & Engineers, pp. 1–5. https://doi.org/10.3997/2214-4609.201800732.
Haapala, I., Rämö, O.T., Frindt, S., 2005. Comparison of proterozoic and phanerozoic rift-related basaltic-granitic magmatism. Lithos 80, 1–32. https://doi.org/10.1016/j.lithos.2004.04.057.
Hallman, S., Fowlkes, C.C., 2015. Oriented edge forests for boundary detection. In: Proceedings of the IEEE Computer Society Conference on Computer Vision and Pattern Recognition, pp. 1732–1740. https://doi.org/10.1109/CVPR.2015.7298782, 07-12-*June*.
Hariharan, B., Arbeláez, P., Girshick, R., Malik, J., 2014. Simultaneous detection and segmentation. In: Lecture Notes in Computer Science (Including Subseries Lecture Notes in Artificial Intelligence and Lecture Notes in Bioinformatics), 8695 LNCS (PART 7), pp. 297–312. https://doi.org/10.1007/978-3-319-10584-0_20.
Hariharan, B., Arbelaez, P., Girshick, R., Malik, J., 2016. Object instance segmentation and fine-grained localization using hypercolumns. IEEE Trans. Pattern Anal. Mach. Intell. 39 (4), 627–639. https://10.1109/TPAMI.2016.2578328.
Havaei, M., Davy, A., Warde-Farley, D., Biard, A., Courville, A., Bengio, Y., Pal, C., Jodoin, P.M., Larochelle, H., 2017. Brain tumor segmentation with deep neural networks. Med. Image Anal. 35, 18–31. https://doi.org/10.1016/j.media.2016.05.004.
He, Kaiming, Zhang, Xiangyu, Ren, Shaoqing, Sun, Jian, 2015. Delving deep into rectifiers: surpassing human-level performance on imagenet classification. In: In Proceedings of the IEEE International Conference on Computer Vision, pp. 1026–1034.
He, K., Gkioxari, G., Dollár, P., Girshick, R., 2017. Mask R-CNN. In: Proceedings of the IEEE International Conference on Computer Vision, pp. 2961–2969. https://doi.org/10.48550/arXiv.1703.06870.
He, X., Zhou, Y., Zhao, J., Zhang, D., Yao, R., Xue, Y., 2022. Swin transformer embedding UNet for remote sensing image semantic segmentation. IEEE Trans. Geosci. Rem. Sens. 60 https://doi.org/10.1109/TGRS.2022.3144165.
Hinton, G., Srivastava, N., Swersky, K., 2012. Neural networks for machine learning lecture 6a overview of mini-batch gradient descent. Lecture notes. Cited on 14 (8), 2. Retrieved from. http://www.cs.toronto.edu/~tijmen/csc321/slides/lecture_slides_lec6.pdf.
Honarmand, M., Shahriari, H., 2021. Geological mapping using drone-based photogrammetry: an application for exploration of vein-type cu mineralization. Minerals 11 (6), 1–13. https://doi.org/10.3390/min11060585.
Hough, P.V., 1962. U.S. Patent No. 3,069,654. U.S. Patent and Trademark Office, Washington, DC.
Iizuka, S., Simo-Serra, E., Ishikawa, H., 2016. Let there be color. ACM Trans. Graph. 35 (4), 1–11. https://doi.org/10.1145/2897824.2925974.
Chollet, F., & others. 2015. Keras. https://keras.io.
Intel ® Hyper-Threading Technology. (n.d.). Intel. https://www.intel.com/content/www/us/en/architecture-and-technology/hyper-threading/hyper-threading-technology.html. Accessed on 5th June 2023.
Jaccard, P., 1912. The distribution of the flora in the alpine zone. New Phytol. 11 (2), 37–50. https://doi.org/10.1111/j.1469-8137.1912.tb05611.x.
Jafrasteh, B., Manighetti, I., Zerubia, J., 2020. Generative adversarial networks as a novel approach for tectonic fault and fracture extraction in high resolution satellite and airborne optical images. In: ISPRS-international Archives of the Photogrammetry, Remote Sensing and Spatial Information Sciences, pp. 1219–1227. https://doi.org/10.5194/isprs-archives-XLIII-B3-2020-1219-2020. XLIII-B3-2020.
James, M.R., 2017, August. SfM-MVS PhotoScan Image Processing Exercise. In: IAVCEI 2017 UAS workshop. Lancaster University.
Junior, A.M., Racolte, G., de Souza, E.M., Domingos, H.V., Horota, R.K., Motta, J.G., Zanotta, D.C., Cazarin, C.L., Gonzaga, L., Veronez, M.R., 2021. Deep learning application for fracture segmentation over outcrop images from uav-based digital photogrammetry. In: International Geoscience and Remote Sensing Symposium (IGARSS), 2021-July, pp. 4692–4695. https://doi.org/10.1109/IGARSS47720.2021.9553232.
Kanoun, B., Cherif, M.A., Manighetti, I., Tarabalka, Y., Zerubia, J., 2022. An enhanced deep learning approach for tectonic fault and fracture extraction in very high resolution optical images. In: ICASSP 2022 – 2022 IEEE International Conference on Acoustics. Speech and Signal Processing (ICASSP), pp. 3403–3407. https://doi.org/10.1109/icassp43922.2022.9747007, 2022.
Kovesi, P., 1997. Symmetry and Asymmetry from Local Phase. Tenth Australian Joint Conference on Artificial Intelligence, vols. 2–4. http://citeseerx.ist.psu.edu/viewdoc/download?doi=10.1.1.40.4146&rep=rep1&type=pdf.
Kovesi, P., 1999. Image features from phase congruency. Videre A J. Comput. Vis. Res. 1 (3), 1–26. Retrieved from. https://citeseerx.ist.psu.edu/viewdoc/download?doi=10.1.1.54.5658&rep=rep1&type=pdf.
Lai, W.S., Huang, J. Bin, Ahuja, N., Yang, M.H., 2017. Deep laplacian pyramid networks for fast and accurate super-resolution. In: Proceedings – 30th IEEE Conference on Computer Vision and Pattern Recognition, pp. 5835–5843. https://doi.org/10.1109/CVPR.2017.618. *CVPR 2017, 2017-January*.
Ledig, C., Theis, L., Huszár, F., Caballero, J., Cunningham, A., Acosta, A., Aitken, A., Tejani, A., Totz, J., Wang, Z., Shi, W., 2017. Photo-realistic single image super-resolution using a generative adversarial network. In: Proceedings – 30th IEEE Conference on Computer Vision and Pattern Recognition, pp. 105–114. https://doi.org/10.1109/CVPR.2017.19. *CVPR 2017, 2017-Januar*y.

Lepage, R., Rouhana, R.G., Onge, B.S., Noumeir, R., Desjardins, R., 2000. Cellular neural network for automated detection of geological lineaments on radarsat images. IEEE Trans. Geosci. Rem. Sens. 38 (3), 1224–1233. https://10.1109/36.843014.

Li, D., Wu, J., He, Y., Yao, X., Yuan, W., Chen, D., Park, H.-C., Yu, S., Prince, J.L., Li, X., 2019. Parallel deep neural networks for endoscopic OCT image segmentation. Biomed. Opt Express 10 (3), 1126. https://doi.org/10.1364/boe.10.001126.

Li, G., Ma, B., He, S., Ren, X., Liu, Q., 2020. Automatic tunnel crack detection based on u-net and a convolutional neural network with alternately updated clique. Sensors 20 (3). https://doi.org/10.3390/s20030717.

Lin, T.Y., Goyal, P., Girshick, R., He, K., Dollár, P., 2017. Focal loss for dense object detection. In: Proceedings of the IEEE International Conference on Computer Vision, pp. 2980–2988.

Lin, L., Zhong, Z., Cai, Z., Sun, A.Y., Li, C.L., 2022. Automatic geological fault identification from seismic data using 2.5D channel attention U-net. Geophysics 87 (4). https://doi.org/10.1190/geo2021-0805.1.

Liu, Y.-C., Chen, C.-S., 2007. A new approach for application of rock mass classification on rock slope stability assessment. Eng. Geol. 89, 129–143. https://doi.org/10.1016/j.enggeo.2006.09.017.

Liu, L., Li, W., Shi, Z., Zou, Z., 2022. Physics-informed hyperspectral remote sensing image synthesis with deep conditional generative adversarial networks. IEEE Trans. Geosci. Rem. Sens. 60, 1–15. https://10.1109/TGRS.2022.3173532.

Lusnig, L., 2020. Ridge detection. Retrieved from. https://pypi.org/project/ridge-detection.

Manighetti, I., Jafrasteh, B., Zerubia, J., 2020. GAN and U-net abilities to automate tectonic fault mapping in remote sensing optical images. AGU Fall Meeting Abstracts 2020. S056-08). Retrieved from. https://ui.adsabs.harvard.edu/abs/2020AGUFMS056...08M/abstract.

Marques, A., Racolte, G., Zanotta, D.C., Menezes, E., Cazarin, C.L., Gonzaga, L., Veronez, M.R., 2022. Adaptive segmentation for discontinuity detection on karstified carbonate outcrop images from UAV-SfM acquisition and detection bias analysis. IEEE Access 10, 20514–20526.

Marr, D., Hildreth, E., 1980. Theory of edge detection. Proceedings of the Royal Society of London. Series B. Biological Sciences 207 (1167), 187–217. https://doi.org/10.1098/rspb.1980.0020.

Mattéo, L., Manighetti, I., Tarabalka, Y., Gaucel, J.M., van den Ende, M., Mercier, A., Tasar, O., Girard, N., Leclerc, F., Giampetro, T., Dominguez, S., Malavieille, J., 2021. Automatic Fault mapping in remote optical images and topographic data with deep learning. Journal of geophysical research. Solid Earth 126 (4), 1–38. https://doi.org/10.1029/2020JB021269.

Microsoft, 2022. December 20. Dv4 and Dsv4-Series - Azure Virtual Machines. Microsoft Learn. https://learn.microsoft.com/en-us/azure/virtual-machines/dv4-dsv4-series#dv4-series. (Accessed 5 June 2023).

Milletari, F., Ahmadi, S.A., Kroll, C., Plate, A., Rozanski, V., Maiostre, J., Levin, J., Dietrich, O., Ertl-Wagner, B., Bötzel, K., Navab, N., 2017. Hough-CNN: deep learning for segmentation of deep brain regions in MRI and ultrasound. Comput. Vis. Image Understand. 164, 92–102. https://doi.org/10.1016/j.cviu.2017.04.002.

Moeskops, P., Wolterink, J.M., van der Velden, B.H.M., Gilhuijs, K.G.A., Leiner, T., Viergever, M.A., Išgum, I., 2016. Deep learning for multi-task medical image segmentation in multiple modalities. In: Lecture Notes in Computer Science (Including Subseries Lecture Notes in Artificial Intelligence and Lecture Notes in Bioinformatics), 9901 LNCS, pp. 478–486. https://doi.org/10.1007/978-3-319-46723-8_55.

Nair, V., Hinton, G.E., 2010. Rectified linear units improve restricted Boltzmann machines. In: In Proceedings of the 27th International Conference on Machine Learning (ICML-10), pp. 807–814. Retrieved from. https://www.cs.toronto.edu/~hinton/absps/reluICML.pdf.

Neuman, S.P., 2005. Trends, prospects and challenges in quantifying flow and transport through fractured rocks. Hydrogeol J. 13, 124–147. https://doi.org/10.1007/s10040-004-0397-2.

Nex, F., Armenakis, C., Cramer, M., Cucci, D.A., Gerke, M., Honkavaara, E., Kukko, A., Persello, C., Skaloud, J., 2022. UAV in the advent of the twenties: where we stand and what is next. ISPRS J. Photogrammetry Remote Sens. 184, 215–242. https://doi.org/10.1016/j.isprsjprs.2021.12.006. January.

Nironen, M., 1997. The Svecofennian Orogen: a tectonic model. Precambrian Res. 86, 21–44. https://doi.org/10.1016/S0301-9268(97)00039-9.

Nordbäck, N., Ovaskainen, N., 2022. UAV-acquired orthomosaics of Loviisa shoreline outcrops (1.0.0) [Data set]. Zenodo. https://doi.org/10.5281/zenodo.7077519.

Nordbäck, N., Ovaskainen, N., Markovaara-Koivisto, M., Skyttä, P., Ojala, A., Engström, J., Nixon, C., 2023. Multiscale interpretation and scaling analysis of the censored brittle structural framework within the crystalline bedrock of southern Finland. Bull. Geol. Soc. Finland 95.

Odling, N.E., Gillespie, P., Bourgine, B., Castaing, C., Chiles, J.P., Christensen, N.P., et al., 1999. Variations in fracture system geometry and their implications for fluid flow in fractures hydrocarbon reservoirs. Petrol. Geosci. 5 (4), 373–384. https://doi.org/10.1144/petgeo.5.4.373.

Ovaskainen, N., 2020. Nikolas Ovaskainen Scalability of Lineament and Fracture Networks within the Crystalline Wiborg Rapakivi Batholith, SE Finland. Master 's Thesis. Turun Yliopisto (University of Turku), Turku, Finland, 2020. Retrieved from. http://urn.fi/URN:NBN:fi-fe202003259211.

Ovaskainen, N., 2022. Fractopo (0.4.0). Zenodo. https://doi.org/10.5281/zenodo.6655890.

Ovaskainen, N., 2023. fractopo: a Python package for fracture network analysis. J. Open Source Softw. 8 (85), 5300. https://doi.org/10.21105/joss.05300.

Ovaskainen, N., Nordbäck, N., 2022. Manually mapped traces from UAV-acquired images of Loviisa shoreline outcrops (1.1.0) [Data set]. Zenodo. https://doi.org/10.5281/zenodo.7077846.

Ovaskainen, N., Nordbäck, N., Skyttä, P., Engström, J., 2022. A new subsampling methodology to optimize the characterization of two-dimensional bedrock fracture networks. J. Struct. Geol. 155 https://doi.org/10.1016/j.jsg.2022.104528. January.

Prabhakaran, R., Bruna, P.O., Bertotti, G., Smeulders, D., 2019. An automated fracture trace detection technique using the complex shearlet transform. Solid Earth 10 (6), 2137–2166. https://doi.org/10.5194/se-10-2137-2019.

Prewitt, J.M.S., 1970. "Object Enhancement and Extraction". Picture Processing and Psychopictorics. Academic Press.

Qiao, W., Zhang, H., Zhu, F., Wu, Q., 2021. A crack identification method for concrete structures using improved U-net convolutional neural networks. Math. Probl Eng. https://doi.org/10.1155/2021/6654996, 2021.

Rämö, O.T., Haapala, I., 2005. Chapter 12 rapakivi granites. In: Developments in Precambrian Geology. Elsevier, pp. 533–562. https://doi.org/10.1016/S0166-2635(05)80013-1.

Redmon, J., Divvala, S., Girshick, R., Farhadi, A., 2016. You only look once: unified, real-time object detection. In: Proceedings of the IEEE Computer Society Conference on Computer Vision and Pattern Recognition, pp. 779–788. https://doi.org/10.1109/CVPR.2016.91. *2016-Decem*.

Ren, S., He, K., Girshick, R., Sun, J., 2017. Faster R-CNN: towards real-time object detection with region proposal networks. IEEE Trans. Pattern Anal. Mach. Intell. 39 (6), 1137–1149. https://doi.org/10.1109/TPAMI.2016.2577031.

Roberts, L.G., 1965. Machine perception of three-dimensional solids. In: Tippett, J.T., Borkowitz, D.A., Clapp, L.C., Koester, C.J., Vanderburgh Jr, A. (Eds.), *Symposium Of Optical And Electro-Optical Information Processing Technology*. Proceedings. Massachusetts Inst of Tech, Cambridge. May 1965.

Rohrbaugh Jr., M.B., Dunne, W.M., Mauldon, M., 2002. Estimating fracture trace intensity, density, and mean length using circular scan lines and windows. AAPG Bull. 86 (12), 2089–2104. https://doi.org/10.1306/61EEDE0E-173E-11D7-8645000102C1865D.

Ronneberger, O., Fischer, P., Brox, T., 2015. U-net: convolutional networks for biomedical image segmentation. In: International Conference on Medical Image Computing and Computer-Assisted Intervention. Springer, Cham, pp. 234–241. https://10.1007/978-3-319-24574-4_28.

Roth, H.R., Shen, C., Oda, H., Oda, M., Hayashi, Y., Misawa, K., Mori, K., 2018. Deep learning and its application to medical image segmentation. Med. imaging Technol. 36 (2), 63–71. https://doi.org/10.11409/mit.36.63.

Samsu, A., Cruden, A.R., Micklethwaite, S., Grose, L., Vollgger, S.A., 2020. Scale matters: the influence of structural inheritance on fracture patterns. J. Struct. Geol. 130, 103896 https://doi.org/10.1016/j.jsg.2019.103896. May 2019.

Sanderson, D.J., Nixon, C.W., 2015. The use of topology in fracture network characterization. J. Struct. Geol. 72, 55–66. https://doi.org/10.1016/j.jsg.2015.01.005.

Sanderson, D.J., Peacock, D.C.P., 2020. Making rose diagrams fit-for-purpose. Earth Sci. Rev. 201, 103055 https://doi.org/10.1016/j.earscirev.2019.103055. November 2019.

Scheiber, T., Fredin, O., Viola, G., Jarna, A., Gasser, D., Łapińska-Viola, R., 2015. Manual extraction of bedrock lineaments from high-resolution LiDAR data: methodological bias and human perception. GFF 137 (4), 362–372. https://doi.org/10.1080/11035897.2015.1085434.

Sefrin, O., Riese, F.M., Keller, S., 2021. Deep learning for land cover change detection. Rem. Sens. 13 (1), 1–27. https://doi.org/10.3390/rs13010078.

Sermanet, P., Eigen, D., Zhang, X., Mathieu, M., Fergus, R., LeCun, Y., 2014. Overfeat: integrated recognition, localization and detection using convolutional networks. In: 2nd International Conference on Learning Representations, ICLR 2014 - Conference Track Proceedings.

Shelhamer, E., Long, J., Darrell, T., 2017. Fully convolutional networks for semantic segmentation. IEEE Trans. Pattern Anal. Mach. Intell. 39 (4), 640–651. https://doi.org/10.1109/TPAMI.2016.2572683.

Skyttä, P., Ovaskainen, N., Nordbäck, N., Engström, J., Mattila, J., 2021. Fault-induced mechanical anisotropy and its effects on fracture patterns in crystalline rocks. J. Struct. Geol. 146 https://doi.org/10.1016/j.jsg.2021.104304. October 2020.

Sobel, I.E., 1970. Camera Models and Machine Perception. Stanford Doctoral Dissertation.

Sobel, I., Feldman, G., 2015. An Isotropic 3x3 Image Gradient Operator. Stanford Artificial Intelligence Project (SAIL), pp. 271–272. Retrieved from. https://www.researchgate.net/publication/239398674_An_Isotropic_3x3_Image_Gradient_Operator.

Steger, G., 1998. An unbiased detector of curvilinear structures. IEEE Trans. Pattern Anal. Mach. Intell. 20 (2), 113–125. https://doi.org/10.1109/34.659930.

Tamminen, J., 2020. Kalliorakojen Automaattinen Mallintaminen Ilmakuvista. Master's Thesis (in Finnish). Turun Yliopisto (University of Turku), Turku, Finland, 2020. Retrieved from. https://www.utupub.fi/bitstream/handle/10024/150615/Tamminen_Jonne_opinnayte.pdf?sequence=1.

Tamminen, J., Ovaskainen, N., 2022. ALSA (0.1.1). Zenodo. https://doi.org/10.5281/zenodo.7081038.

Tanimoto, T., 1958. An Elementary Mathematical Theory of Classification and Prediction. International Business Machines Corporation, New York, pp. 1–10.

Thiele, S.T., Grose, L., Samsu, A., Micklethwaite, S., Vollgger, S.A., Cruden, A.R., 2017. Rapid, semi-automatic fracture and contact mapping for point clouds, images and geophysical data. Solid Earth 8 (6), 1241–1253. https://doi.org/10.5194/se-8-1241-2017.

Thiele, S.T., Grose, L., Cui, T., Cruden, A.R., Micklethwaite, S., 2019. Extraction of high-resolution structural orientations from digital data: a Bayesian approach. J. Struct. Geol. 122, 106–115. https://doi.org/10.1016/j.jsg.2019.03.001. December 2018.

Tieleman, T., Hinton, G., 2012. Lecture 6.5-rmsprop: divide the gradient by a running average of its recent magnitude. COURSERA: Neural networks for machine learning. Intell. Control Autom. 4 (2), 26–31.

Tingdahl, K.M., De Rooij, M., 2005. Semi-automatic detection of faults in 3D seismic data. Geophys. Prospect. 53 (4), 533–542. https://doi.org/10.1111/j.1365-2478.2005.00489.x.

Turner, D., Lucieer, A., Watson, C., 2012. An automated technique for generating georectified mosaics from ultra-high resolution Unmanned Aerial Vehicle (UAV) imagery, based on Structure from Motion (SFM) point clouds. Rem. Sens. 4 (5), 1392–1410. https://doi.org/10.3390/rs4051392.

Tversky, A., 1977. Features of similarity. - 1977 - Tversky.pdf. Psychol. Rev. 84 (4), 327–352. https://doi.org/10.1037/0033-295X.84.4.327.

Urbanowicz, R.J., Moore, J.H., 2015. ExSTraCS 2.0: description and evaluation of a scalable learning classifier system. Evolutionary Intelligence 8 (2–3), 89–116. https://doi.org/10.1007/s12065-015-0128-8.

Vaasjoki, M., Tapani Rämö, O., Sakko, M., 1991. New U-Pb ages from the Wiborg rapakivi area: constraints on the temporal evolution of the rapakivi granite-anorthosite-diabase dyke association of southeastern Finland. Precambrian Res. 51, 227–243. https://doi.org/10.1016/0301-9268(91)90102-G.

Van Oord, A., Kalchbrenner, N., Kavukcuoglu, K., 2016. Pixel recurrent neural networks. In: International Conference on Machine Learning. PMLR, pp. 1747–1756.

Varghese, A., Gubbi, J., Ramaswamy, A., Balamuralidhar, P., 2019. ChangeNet: a deep learning architecture for visual change detection. Lect. Notes Comput. Sci. 11130 LNCS, 129–145. https://doi.org/10.1007/978-3-030-11012-3_10. January.

Vasuki, Y., Holden, E.J., Kovesi, P., Micklethwaite, S., 2014. Semi-automatic mapping of geological Structures using UAV-based photogrammetric data: an image analysis approach. Comput. Geosci. 69, 22–32. https://doi.org/10.1016/j.cageo.2014.04.012.

Vincent, O., Folorunso, O., 2009. A descriptive algorithm for Sobel image edge detection. In: Proceedings of the 2009 InSITE Conference. https://doi.org/10.28945/3351.

Wang, W., Liao, H., Huang, Y., 2007. Rock fracture tracing based on image processing and SVM. In: Third International Conference on Natural Computation (ICNC 2007), vol. 1. IEEE, pp. 632–635.

Wang, G., Dong, G., Li, H., Han, L., Tao, X., Ren, P., 2019. Remote sensing image synthesis via graphical generative adversarial networks. In: IGARSS 2019-2019 IEEE International Geoscience and Remote Sensing Symposium. IEEE, pp. 10027–10030. https://10.1109/IGARSS.2019.8898915.

Weldon, T.P., Higgins, W.E., Dunn, D.F., 1996. Efficient Gabor filter design for texture segmentation. Pattern Recogn. 29 (12), 2005–2015. https://doi.org/10.1016/S0031-3203(96)00047-7.

Wu, X., Fomel, S., 2018. Automatic fault interpretation with optimal surface voting. Geophysics 83 (5), O67–O82. https://doi.org/10.1190/geo2018-0115.1.

Wu, J., Shi, Y., Wang, W., 2022. Fault imaging of seismic data based on a modified U-net with dilated convolution. Appl. Sci. 12 (5) https://doi.org/10.3390/app12052451.

Zeeb, C., Gomez-Rivas, E., Bons, P.D., Blum, P., 2013. Evaluation of sampling methods for fracture network characterization using outcrops. AAPG Bull. 97 (9), 1545–1566. https://doi.org/10.1306/02131312042.

Zhang, R., Isola, P., Efros, A.A., 2016. Colorful Image Colorization. Lecture Notes in Computer Science (Including Subseries Lecture Notes in Artificial Intelligence and Lecture Notes in Bioinformatics), 9907 LNCS, pp. 649–666. https://doi.org/10.1007/978-3-319-46487-9_40.

Zhang, Q., Wang, H., Lu, H., Won, D., Yoon, S.W., 2018. Medical image synthesis with generative adversarial networks for tissue recognition. In: 2018 IEEE International Conference on Healthcare Informatics (ICHI). IEEE, pp. 199–207. https://10.1109/ICHI.2018.00030.

Zhang, Q., Yusifov, A., Joy, C., Shi, Y., Wu, X., 2019. FaultNet: a deep CNN model for 3D automated fault picking, 2019. In: SEG International Exposition and Annual Meeting. Technical Program Expanded Abstracts. Society of Exploration Geophysicists, pp. 2413–2417. https://doi.org/10.1190/segam2019-3215930.1. OnePetro.